

Moderated Neutron Detector for Accumulated Ambient Dose
Equivalent in Proton Therapy



Mr. Tanawat Tawonwong

จุฬาลงกรณ์มหาวิทยาลัย
CHULALONGKORN UNIVERSITY

A Dissertation Submitted in Partial Fulfillment of the Requirements
for the Degree of Doctor of Philosophy in Medical Physics
Department of Radiology
FACULTY OF MEDICINE
Chulalongkorn University
Academic Year 2021
Copyright of Chulalongkorn University



จุฬาลงกรณ์มหาวิทยาลัย
CHULALONGKORN UNIVERSITY



จุฬาลงกรณ์มหาวิทยาลัย
CHULALONGKORN UNIVERSITY

หัววัดนิวตรอนแบบปรับแต่งพลังงานสำหรับการวัดปริมาณรังสีสมมูล โดยรอบในเครื่องฉายรังสี
ด้วยอนุภาคโปรตอน



วิทยานิพนธ์นี้เป็นส่วนหนึ่งของการศึกษาตามหลักสูตรปริญญาวิทยาศาสตรดุษฎีบัณฑิต
สาขาวิชาฟิสิกส์การแพทย์ ภาควิชารังสีวิทยา
คณะแพทยศาสตร์ จุฬาลงกรณ์มหาวิทยาลัย
ปีการศึกษา 2564
ลิขสิทธิ์ของจุฬาลงกรณ์มหาวิทยาลัย

Thesis Title	Moderated Neutron Detector for Accumulated Ambient Dose Equivalent in Proton Therapy
By	Mr. Tanawat Tawonwong
Field of Study	Medical Physics
Thesis Advisor	Taweap Sanghangthum, Ph.D.

Accepted by the FACULTY OF MEDICINE,
Chulalongkorn University in Partial Fulfillment of the
Requirement for the Doctor of Philosophy

..... Dean of the FACULTY
OF MEDICINE
(CHANCHAI SITTIPUNT)

DISSERTATION COMMITTEE

..... Chairman
(Associate Professor SIVALEE
SURIYAPEE)

..... Thesis Advisor
(Taweap Sanghangthum, Ph.D.)

..... Examiner
(Associate Professor KANJANA
SHOTELERSUK, M.D.)

..... Examiner
(KITIWAT KHAMWAN)

..... External Examiner
(Kosuke Matsubara)

ธนวัฒน์ ถาวรวงษ์ : หัววัดนิวตรอนแบบปรับแต่งพลังงานสำหรับการวัดปริมาณรังสีสะสมโดยรอบในเครื่องฉายรังสีด้วยอนุภาคโปรตอน. (Moderated Neutron Detector for Accumulated Ambient Dose Equivalent in Proton Therapy) อ.ที่ปรึกษาหลัก : อ. ดร.ทวีป แสงแห่งธรรม

เครื่องฉายรังสีด้วยอนุภาคโปรตอนขนาดเล็กได้ถูกติดตั้ง ณ ศูนย์โปรตอนสมเด็จพระเทพรัตนราชสุดาฯ โรงพยาบาลจุฬาลงกรณ์ สภากาชาดไทย โครงการเริ่มต้นขึ้นในปี พ.ศ. 2561 และใช้เวลารวมทั้งสิ้น 4 ปี แม้ในช่วงเวลาที่มีการระบาดของโรคโควิด 19 ผู้ป่วยรายแรกได้รับการรักษาด้วยอนุภาคโปรตอน ในเดือนสิงหาคม พ.ศ. 2564 ในส่วนของความปลอดภัยทางรังสีของศูนย์โปรตอนสมเด็จพระเทพรัตนราชสุดาฯ นั้น โครงสร้างของอาคารได้ผ่านการคำนวณความสามารถในการกักรังสีก่อนทำการจัดสร้าง และผ่านการสำรวจวัดปริมาณรังสีสะสมโดยรอบ ณ ช่วงเวลาที่ทำการติดตั้งเครื่องไซโคลตรอน และช่วงเวลาของการใช้ลำอนุภาคโปรตอนในห้องทำการรักษา ด้วยเครื่องมือวัดรังสีนิวตรอนชนิด WENDI-II ซึ่งเป็นที่ยอมรับในระดับสากลและทางศูนย์โปรตอนฯ มีอยู่เพียงเครื่องเดียว วัตถุประสงค์ของงานวิจัยนี้คือการจัดสร้างเครื่องมือวัดรังสีนิวตรอนแบบปรับแต่งพลังงานสำหรับอุปกรณ์นับวัดชนิด CR-39 และตรวจสอบประสิทธิภาพการใช้งานผ่านการวัดปริมาณรังสีสะสมโดยรอบ $H^*(10)$ โดยขอตั้งชื่ออุปกรณ์นี้ว่า อุปกรณ์นับวัดปริมาณรังสีนิวตรอน โดยรอบแบบปรับแต่งพลังงานจากจุฬาลงกรณ์มหาวิทยาลัย (CUMOD) ทั้งนี้ CUMOD นั้นได้รับการออกแบบเพื่อให้ใช้กับเครื่องเร่งอนุภาคโปรตอนที่มีพลังงานสูงสุด 250 เมกะอิเล็กตรอนโวลต์ ด้วยเทคนิคการให้รังสีแบบ pencil beam scanning (PBS) โปรแกรมจำลองทางคณิตศาสตร์ PHITS ถูกใช้ในการคำนวณหารูปแบบการตอบสนองต่อช่วงพลังงานของรังสีนิวตรอน การสอบเทียบค่า $H^*(10)$ ของ CUMOD นั้น ทำโดยใช้ต้นกำเนิดรังสีนิวตรอนชนิด อะเมริเซียมกับเบริลเลียม ในช่วง 100 ถึง 1000 ไมโครซีเวิร์ด สำหรับการวัด $H^*(10)$ นั้น ใช้ศูนย์โปรตอนฯ นั้น ค่าที่ได้จะถูกนำไปเปรียบเทียบกับค่าที่ได้จากหัววัด WENDI-II โดยความหลากหลายทางพลังงานของนิวตรอนที่ทำการวัดนั้น ได้มาจากการกำหนดรูปแบบของลำอนุภาคโปรตอนที่มีการกระจายของปริมาณรังสีของอนุภาคโปรตอนที่ครอบคลุมทุกช่วงการรักษาทางคลินิก โดยพบว่าค่า $H^*(10)$ ที่ได้จาก CUMOD และ WENDI-II มีความสัมพันธ์กันแบบเส้นตรง โดยมีค่าสัมประสิทธิ์อยู่ที่ 0.64 ทั้งนี้เพื่อการเปรียบเทียบกับงานวิจัยอื่นๆ ได้คำนวณค่า $H^*(10)$ ต่อปริมาณรังสีที่ทำการรักษา 1 เกรย์ ของ CUMOD ได้ในช่วง 0.018 ถึง 0.105 มิลลิซีเวิร์ดต่อเกรย์ สำหรับขนาดลำรังสี 10 คูณ 10 ตารางเซนติเมตร ที่ระยะ 1 เมตร จากผลของงานวิจัยนี้พบว่า CUMOD สามารถใช้วัดปริมาณรังสี $H^*(10)$ ได้ในหลายตำแหน่งพร้อมๆ กัน เพิ่มเติมจากการใช้งานเฉพาะหัววัด WENDI-II

จุฬาลงกรณ์มหาวิทยาลัย
CHULALONGKORN UNIVERSITY

สาขาวิชา ฟิสิกส์การแพทย์
ปีการศึกษา 2564

ลายมือชื่อนิสิต
ลายมือชื่อ อ.ที่ปรึกษาหลัก

5974763630 : MAJOR MEDICAL PHYSICS

KEYWOR Ambient dose equivalent, Proton therapy, WENDI-II, CUMOD,
D: neutron detector

Tanawat Tawonwong : Moderated Neutron Detector for Accumulated Ambient Dose Equivalent in Proton Therapy. Advisor: Taweap Sanghangthum, Ph.D.

The Varian ProBeam compact was installed at Her Royal Highness Princess Maha Chakri Sirindhorn Proton Center. Since 2017, the project has started at the King Chulalongkorn Memorial Hospital and after 4 years, during Covid19 pandemic, the 1st patient treatment received proton therapy on August, 2021. The radiation safety of the center was accomplished through firstly, the shielding calculation and secondary, the radiation survey at the milestone points such as cyclotron installation and 1st Beam ON at the treatment room. The only one WENDI-II dosimeter was used in radiation survey. The main purpose of this study is to validate the in-house neutron moderator based on CR-39 detector, Chulalongkorn University Neutron Moderator (CUMOD) through the ambient dose equivalent measurement, $H^*(10)$ and designed to use with proton pencil beam scanning, PBS of energy up to 250 MeV. The PHITS MC was used to simulate the neutron response function of CUMOD. The calibration of CUMOD was performed using $^{241}\text{AmBe}$ source in the range of 100 to 1000 μSv . The $H^*(10)$ from CUMOD were compared with the one from WENDI-II. The variation of neutron fields was generated from various proton plans to cover most of the clinical scenarios. The linearly relationship between CUMOD and WENDI-II was observed with the factor of 0.64. The $H^*(10)$ per therapeutic dose was in the range of 0.018 to 0.105 mSv/Gy for $10 * 10 \text{ cm}^2$ at 1 m distance. The advantage of CUMODs is the ability to measure $H^*(10)$ in various positions instantaneously.

จุฬาลงกรณ์มหาวิทยาลัย
CHULALONGKORN UNIVERSITY

Field of Study: Medical Physics

Student's Signature

Academic 2021

Advisor's Signature

Year:

.....

ACKNOWLEDGEMENTS

I would like to express my heartfelt gratitude to my mentor, Assoc. Prof. Sivalee Suriyapee who generously supported me and provided me plenty amount of time and opportunities.

I would like to express my great appreciation my advisor, Asst. Prof. Taweap Sanghangthum for his unfailing support and supervise for the whole stage of dissertation from sharing ideas and knowledge, planning and executing experiments, to thesis reviewing.

I would like to acknowledge and thank to thesis committees Assoc. Prof. Kanjana Shotelersuk, Prof. Kosuke Matsubara and Asst. Prof. Kitiwat Khamwan, for their valuable comments. Assistance provided by Assoc. Prof. Anchali Krisanachinda was greatly appreciated.

I gratefully acknowledge the financial support from The Thai Red cross Society for studying this program and extending the training at GSI Helmholtzzentrum für Schwerionenforschung, Darmstadt, Germany.

I would like to offer my special thanks to Dr. Ulrich Weber and Dr. Felix Horst, the supervisor and friend of Biophysics, GSI for the wonderful and unforgettably excursion in Frankfurt and Marburg.

I would also like to thank Dr. Thiansin Liamsuwan from Chulabhorn Royal Academy for her great support with the PHITS Monte Carlo simulation.

I would like to thankfully acknowledge my colleagues, staff and faculty members – Jaruek Kanphet, Dr. Sirinya Raungchan, Dr. Sornjarod Oonsiri and many others who played an integral part in my dissertation.

A very special thanks goes out to the Nuclear and Radiation Metrology Section, Office of Atoms for Peace, particularly to Dr. Vithit Pungkun and Tanapol Dachviriyakij, who permitted and supported me to use the CR-39 detectors and neutron source calibrator.

Last, but not least, I dedicate my dissertation work to my wife, Sasivimol Promma whose love and support lifted me from start to finish; my mother, Malee Tawonwong who always sacrificed herself for the well-being of her son; my father and mother in-law, Latthi and Patcharee Promma who always stayed and supported; my two

elder sisters, Meatrawee and Pattanachat Tawonwong who always looked after their younger brother, and to beloved daughter, Alinda Tawonwong whose always love and sent her father the power.

Tanawat Tawonwong

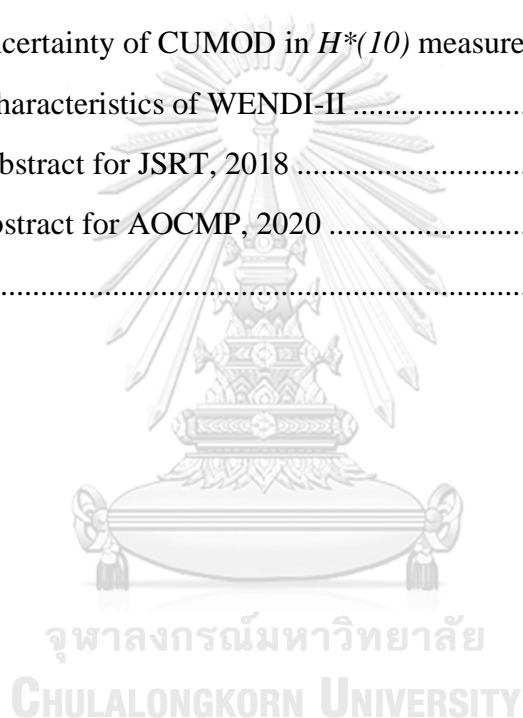


TABLE OF CONTENTS

	Page
.....	iii
ABSTRACT (THAI)	iii
.....	iv
ABSTRACT (ENGLISH)	iv
ACKNOWLEDGEMENTS	v
TABLE OF CONTENTS	vii
LIST OF TABLES	x
LIST OF FIGURES	xi
CHAPTER 1 INTRODUCTION	1
CHAPTER 2 REVIEWS OF RELATED LITERATURE.....	3
2.1 Theory.....	3
2.1.1 Proton therapy	3
2.1.1.1 Interaction of proton with matter.....	4
2.1.1.2 Shielding for proton therapy.....	6
2.1.2 Secondary radiation: Neutron.....	9
2.1.2.1 Neutron classification.....	9
2.1.2.2 Interaction of neutron with matter.....	10
2.1.2.3 Neutron dosimetry	11
2.1.3 Ambient dose equivalent	11
2.1.4 Neutron detection	12
2.1.5 Polyallyl diglycol carbonate (PADC), CR-39	13
2.1.6 Neutron moderator types	14
2.2 Literature review.....	15
CHAPTER 3 RESEARCH METHODOLOGY	19
3.1 Research question	19

3.2 Research objective	19
3.3 Research design	19
3.4 Conceptual framework.....	19
3.5 Research design model	20
3.6 Expected benefit	20
3.7 Variable measurement	21
3.8 Data collection.....	21
3.9 Data analysis	21
3.10 Outcome.....	21
3.11 Statistical analysis.....	21
3.12 Ethical consideration.....	21
CHAPTER 4 MATERIALS AND METHODS	23
4.1 Materials	23
4.1.1 ProBeam® compact single-room proton therapy.....	23
4.1.2 Neutron sources	24
4.1.3 Wide-Energy Neutron Detection Instrument (WENDI-2).....	25
4.1.4 CR-39	26
4.1.5 Etching water bath.....	26
4.1.6 TASLIMAGE automatic reader system.....	27
4.1.7 Moderator materials	28
4.1.8 Solid water phantom.....	28
4.2 Methods	30
4.2.1 Design and create the moderated neutron dosimeter.....	30
4.2.2 Calibration of CUMOD neutron detector.....	30
4.2.3 Simulation of CUMOD response function.....	31
4.2.4 Validation of CUMOD response function.....	31
4.2.5 Ambient dose equivalent measurements	33
CHAPTER 5 RESULTS	36
5.1 Design and create the moderated neutron dosimeter	36

5.2 Calibration of CUMOD	36
5.3 Simulation of CUMOD response function	38
5.4 Validation of CUMOD response function	42
5.5 Ambient dose equivalent measurements.....	46
CHAPTER 6 DISCUSSION.....	48
CHAPTER 7 CONCLUSIONS	52
REFERENCES	53
APPENDIX I Data of CUMOD for PHITS.....	55
APPENDIX II Uncertainty of CUMOD in $H^*(10)$ measurement.....	57
APPENDIX III Characteristics of WENDI-II	58
APPENDIX IV Abstract for JSRT, 2018	62
APPENDIX V Abstract for AOCMP, 2020	63
VITA.....	64



LIST OF TABLES

	Page
Table 2.1 Examples of the shielding goal	7
Table 2.2 Neutron energy classification	9
Table 2.3 The example of neutron cross-sections.....	14
Table 4.1 The interested clinical beam parameters.....	23
Table 5.1 The H*(10) and no. of tracks in the CUMOD calibration process.....	37
Table 5.2 The raw data for CUMOD response function.....	40
Table 5.3 The ambient dose equivalent from WENDI-II and CUMOD for single energy dose plane and multiple energy volume.....	46
Table 5.4 The ambient dose equivalent from WENDI-II and CUMOD for single energy dose plane with variation on the proton dose.....	47
Table 6.1 The comparison of the ambient dose equivalent per therapeutic dose from WENDI-II and CUMOD to Charyyev et al.....	51
Table III.1 The Long-term stability of WENDI-II over 9 months.....	60
Table III.2 The WENDI-II H*(10) results for inverse square law testing.....	61

LIST OF FIGURES

	Page
Figure 1.1 The ProBeam compact single-room proton therapy.....	1
Figure 2.1 Depth dose distribution of pristine bragg peak (Red), spread-out bragg peak (Green), 8 MeV photon beam (Yellow) and 20 MeV electron beam (Blue).	3
Figure 2.2 The cranio-spinal irradiation dose distribution of photon with Conventional, IMRT technique and proton therapy	4
Figure 2.3 The classical impact parameter, b , defined as the closest distance between the initial trajectory of incident proton and the nucleus comparing with the atomic radius, a	6
Figure 2.4 Application of the line-of-sight models to simple bulk shielding geometries.....	8
Figure 2.5 Categories of neutron interaction. The first letter in parenthesis shows the incoming and the second one for outgoing particles	10
Figure 2.6 The concept of the ambient dose equivalent $H^*(10)$	11
Figure 2.7 Fluence-to- $H^*(10)$ conversion coefficients (up to 200 MeV).....	12
Figure 2.8 Miscellany of recoil proton tracks.....	13
Figure 2.9 An averaged calculated response function, solid line, from FLUKA and MCNP.	15
Figure 2.10 The layout of the dosimeters and the simulated response function.....	16
Figure 2.11 The schema of experimental setup at RPTC	17
Figure 3.1 The conceptual framework.....	19
Figure 3.2 The research design model	20
Figure 3.3 The certificate of approval from the Institutional Review	22
Figure 4.1 The layout of our center. Building section (Top). Treatment floor (Bottom)	24
Figure 4.2 The $^{241}\text{AmBe}$ calibrator source and the schematic	24
Figure 4.3 Cutaway view of the WENDI-2 and WENDI-2 connected to a survey meter	25
Figure 4.4 The whole plate and after cutting of CR-39	26

Figure 4.5 The water bath (Right) and the etch and scanning frame (Left).....	27
Figure 4.6 TASLIMAGE automatic reader system	27
Figure 4.7 The 5% borated polyethylene (Right) and Cerrobend alloy (Left)	28
Figure 4.8 The solid water phantom and its orientation according to the proton plans	29
Figure 4.9 Map of models recommended to use in PHITS.....	29
Figure 4.10 The design of CUMOD side view(left) and top view (right)	30
Figure 4.11 The calibration of CUMOD at 100 cm from the ²⁴¹ AmBe calibrator source	31
Figure 4.12 Schematic diagram of the measurement location and the 15 MeV linac neutron spectrum.....	32
Figure 4.13 The measurement of H*(10) of CUMOD and WENDI-II at Varian clinac 23EX for fast neutron response function validation.	32
Figure 4.14 The neutron spectrum of 140 MeV and 200 MeV, the red line presents the 45 degree measurements.	33
Figure 4.15 The measurement of H*(10) of CUMOD and WENDI-II at proton therapy for high energy neutron response function validation.	33
Figure 4.16 The ambient dose equivalent measurement setup at 0 degree at 100 cm distance from isocenter, Wendi-II (Right) and CUMOD (Left)	34
Figure 4.17 The dose distribution of plane dose (left) and volume dose (right)	35
Figure 5.1 The Chulalongkorn University Neutron Moderator (CUMOD)	36
Figure 5.2 The characteristic of the particle tracks from different H*(10).....	37
Figure 5.3 The linear relationship between number of tracks and H*(10)	38
Figure 5.4 The geometry of CUMOD in PHITS	38
Figure 5.5 The example picture of the neutron source and CUMOD in PHITS	39
Figure 5.6 The response function of CUMOD and CR-39 from PHITS	41
Figure 5.7 The reported neutron spectrum up to 15 MeV with percent different of CUMOD response function, the inlay picture shows the approximation of different percentage	42
Figure 5.8 The CUMOD H*(10) result from 15 MeV linaca	43

Figure 5.9 The reported neutron spectrum up to 140 MeV with percent different of CUMOD response function, the inlay picture shows the approximation of different percentage	44
Figure 5.10 The CUMOD H*(10) result from irradiated with 140 MeV proton beam for the field size of 11 * 11 cm ²	44
Figure 5.11 The reported neutron spectrum up to 200 MeV with percent different of CUMOD response function, the inlay picture shows the approximation of different percentage	45
Figure 5.12 The CUMOD H*(10) result from irradiated with 200 MeV proton beam for the field size of 11 × 11 cm ² (30 Gy)	45
Figure 5.13 The characteristic of the particle tracks from different plan types	46
Figure 6.1 The response function of CUMOD (circle), H*(10) conversion coefficient (diamond) and WENDI-II (cross)	48
Figure 6.2 The linear relationship H*(10) between WENDI-II and CUMOD	49
Figure 6.3 The validation results of CUMOD neutron response function	50
Figure III.1 The setup of WENDI-II and ²⁴¹ AmBe (Right) and the linearity results (Left)	58
Figure III.2 The results of dose rate dependence. The inlay table presents the difference percentage.	59
Figure III.3 The setup for angular dependence study	59
Figure III.4 The polar chart represents the angular dependence	60
Figure III.5 The setup of WENDI-II at 100, 300 and 500 cm from isocenter	61

CHAPTER 1 INTRODUCTION

The compact proton therapy, single rotating gantry is installed at the Her Royal Highness Princess Maha Chakri Sirindhorn Proton Center, Bangkok, Thailand. The first patient treatment was started in August 2021. The composition of the system is shown in Figure 1.1. During the beam production, transportation and irradiation, the loss of the proton energy generates the secondary radiation, which need to be concerned for the radiation protection including the shielding calculation as well as estimation of the secondary cancer in patients.

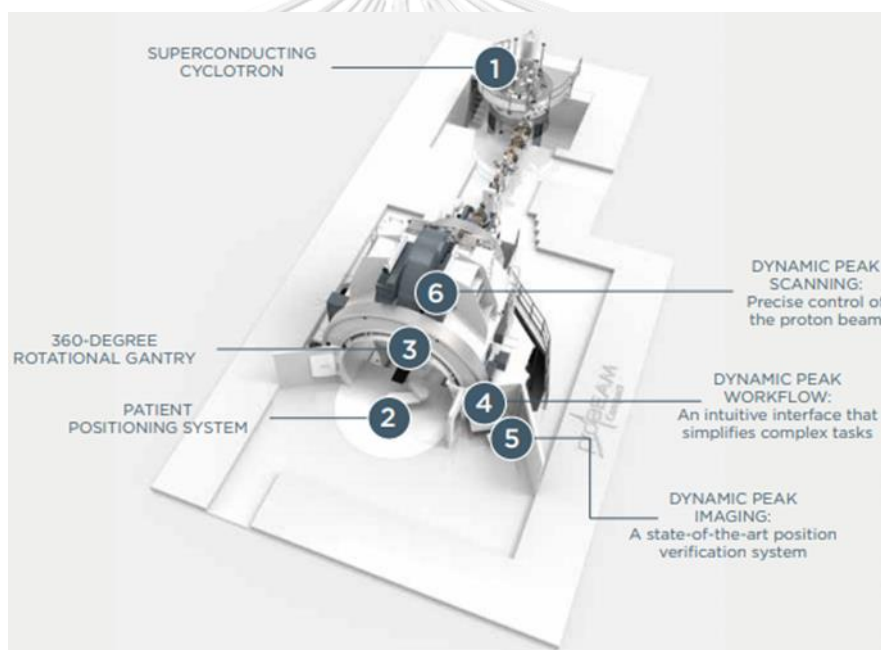


Figure 1.1 The ProBeam compact single-room proton therapy

In proton therapy, neutron is the main component of the secondary radiations⁽¹⁾ due to its characteristics of high radiation weighting factor. The operational quantities ambient dose equivalent $H^*(10)$, has been used to characterize the radiation area monitoring. The $H^*(10)$ from neutron can be obtained by multiplying the fluence-to-ambient dose equivalent conversion coefficients⁽²⁾ to the measured neutron fluence. To measure the neutron $H^*(10)$ in proton therapy, the

response of the dosimeter to the wide neutron energy range is necessary. Many detectors have their own neutron moderator ⁽³⁻⁷⁾ which designed to expand their detector response function matched well with the fluence-to-ambient dose equivalent conversion coefficients. The aim of this study is to create and validate the new moderated neutron detector for the determination of the accumulated ambient dose equivalent, $H^*(10)$, in proton therapy.



CHAPTER 2

REVIEWS OF RELATED LITERATURE

2.1 Theory

2.1.1 Proton therapy

Protons have different dosimetric characteristics compare to photons which employed in conventional radiation therapy. After a short build-up region, conventional radiation shows an exponentially decreasing energy deposition with increasing depth in tissue. In contrast, protons show an increasing energy deposition with penetration distance leading to a maximum (the “Bragg peak”) near the end of range of the proton beam⁽⁸⁾. The characteristics of Pristine Bragg peak and SOBP compared to photon depth dose distribution are shown in Figure 2.1.

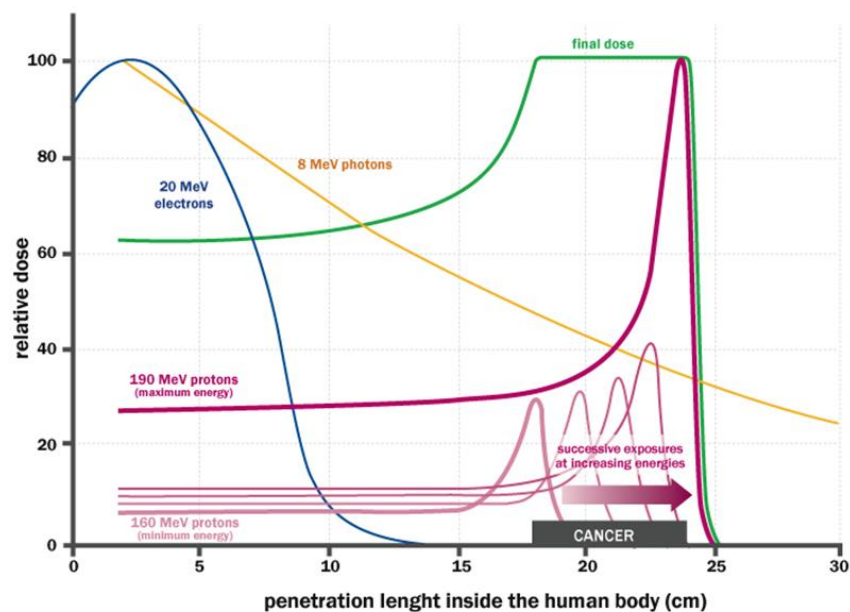


Figure 2.1 Depth dose distribution of pristine bragg peak (Red), spread-out bragg peak (Green), 8 MeV photon beam (Yellow) and 20 MeV electron beam (Blue).

The rationale for the clinical use of proton beams is the feasibility of delivering higher doses to the tumor, leading to an increased tumor control probability (TCP)⁽⁹⁾. This is possible due to the reduced treatment volume and a lower integral dose; patient tolerance is increased. Proton therapy is of particular interest for those tumors located close to serially organized tissues where a small local overdose can cause fatal complication such as most tumors close to the spinal cord. Irregular shaped lesions near critical structures are well suited for protons. Proton therapy has been applied for the treatment of various disease sites⁽¹⁰⁾ and the treatment plan comparisons show that protons offer potential gains for many sites. The cranio-spinal irradiation dose distribution of the proton therapy compared with photon therapy in both Conventional and Intensity Moderated Radiotherapy Therapy (IMRT) technique is illustrated in Figure 2.2.

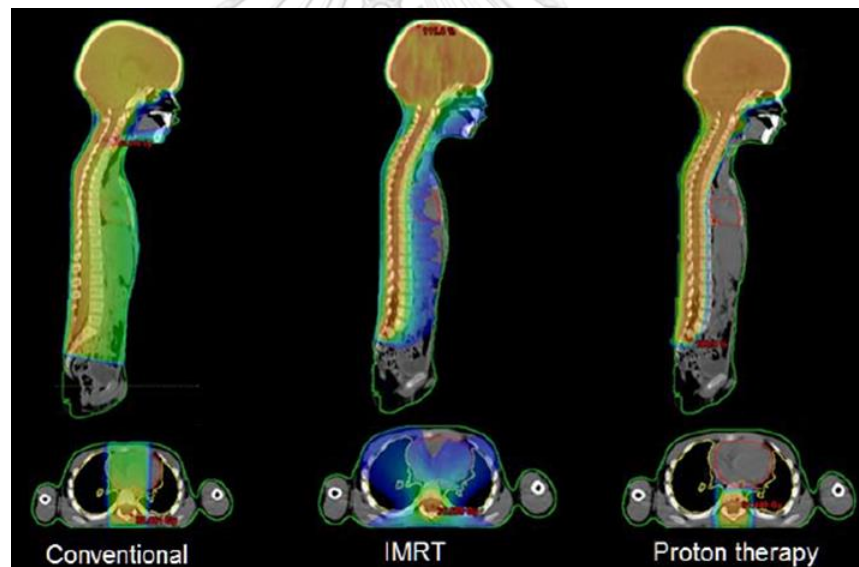


Figure 2.2 The cranio-spinal irradiation dose distribution of photon with Conventional, IMRT technique and proton therapy

2.1.1.1 Interaction of proton with matter

Radiation can interact with matter in different ways depending on the medium but also by the nature and energy of the radiation itself. Radiation can be divided into two categories: charged particle radiation and uncharged radiation. The charged particle radiation includes heavy charged particles, fast electrons and positrons. The uncharged radiation includes photons and neutrons. When radiation interacts with the matter an energy transfer takes place. If this energy is sufficient to

ionize, i.e., to free one or more electrons from the atoms of the medium to which it was bound, the radiation is called ionizing, otherwise it will be called non-ionizing and, in this case, the transferred energy is used to promote an electron to an excited state.

When the radiation causes ionization in a direct and continuous way it is called directly ionizing. Charged particles that interact with the electrons of the medium through Coulombian forces belong to this category. Radiation is indirectly ionizing when the ionization process is mediated by secondary charged particles produced by the interaction of incident radiation with the medium, as in the case of neutrons. In this section we briefly discuss the interaction of radiation with matter, focusing our attention on protons and neutrons.

Protons are charged particles that are heavy compared to electrons, but light compared to most other ions. Their basic modes of interaction with matter are mainly due to the Coulomb interactions⁽¹¹⁾. The probability of a nuclear interaction and the amount of energy transfer per unit depth are much larger than that of an electron.

Protons interact with atomic electrons or with the nuclei along the track in a medium. Since the electrons in solid matter are mostly bound to atoms, interactions do not occur much with electron far from the proton track. Proton interactions are categorized as a function of the classical impact parameter, b , defined as the closest distance between the initial trajectory of incident proton and the nucleus, by comparing b with the atomic radius, a , as illustrated in Figure 2.3.

Interactions with electrons

When $b \gg a$, the incident proton interacts with whole atom, and only a small amount of energy is transferred to atom. These interactions are often called soft collisions. The energy transfer can result in atomic excitation or ionization.

When $b \approx a$, the incident proton can interact with a single orbital electron, resulting in a large energy transfer to that electron, termed a “knock-on electron”. These interactions are often called hard collision. The knock-on electrons ejected from the atom are also termed delta rays.

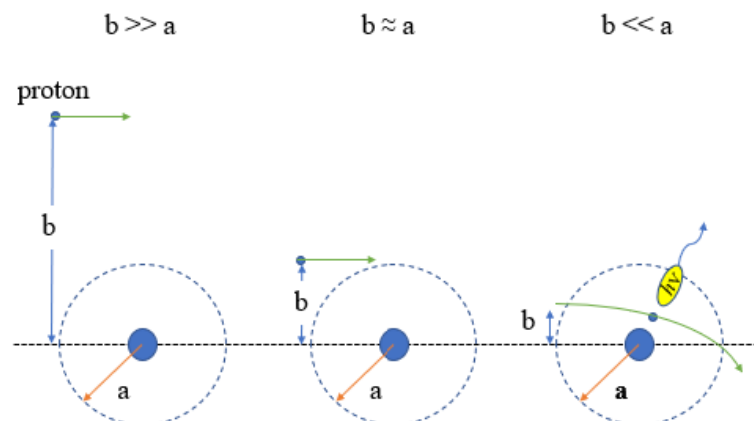


Figure 2.3 The classical impact parameter, b , defined as the closest distance between the initial trajectory of incident proton and the nucleus comparing with the atomic radius, a

Interaction with nucleus

When $b \ll a$, the incident proton interacts with the nucleus via elastic and non-elastic interactions. Elastic scattering can result in large angular deflections, often with limited energy transfer to the target nucleus due to the ratio of the mass between proton and target nucleus. Their contribution is accounted for the consideration of the attenuation of the primary proton beam and additions to the secondary particle fluence.

2.1.1.2 Shielding for proton therapy

Shielding calculation are performed to ensure that the facility designed to facilitate the exposure of staff and public are well within regulatory limits. The shielding calculation of the proton therapy facility can be achieved by two methods. The analytical method, based on the published measurement data and Monte Carlo (MC) simulation data. The result is mostly over-estimate. The full MC simulation method works better, however, the accuracy of the results was depended on the input of simulation. To simulate the whole facility, the details of building and machine, the high-performance computer and long simulation time are needed. The analytical might be used in the planning stage and followed by MC simulation for the last step.

The examples of the shielding goal are demonstrated in Table 2.1.

Table 2.1 Examples of the shielding goal

Area	USA	Japan	Germany	Our center
Controlled	≤ 5 mSv/y	< 1.3 mSv/3mo	20 μ Sv/week (but < 3 mSv/h IDR)	< 5 mSv/y
Public	≤ 1 mSv/y, (20 μ Sv in any one hour)	< 250 μ Sv/3mo (Outside of site boundary)	< 1 mSv/y	< 1 mSv/y (20 μ Sv in any one hour)

For analytical methods, most model consist of line-of-sight models, shown in Figure 2.4, which incorporate the following parameters and assumptions:

- a. Point loss
- b. Distance of the point source to reference point (r)
- c. Angle of the incident beam (line) and the direction to the reference point (θ)
- d. Angular specific source term $H_0(E_p, \theta)$ which depends on the ion type and target type, as well as E_p , the particle energy
- e. Exponential attenuation in shielding material of thickness d_0 , where d is the slant thickness, and $\lambda(\theta)$ is the attenuation length. λ depends on the angle θ because the neutron energy distribution changes with the angle θ

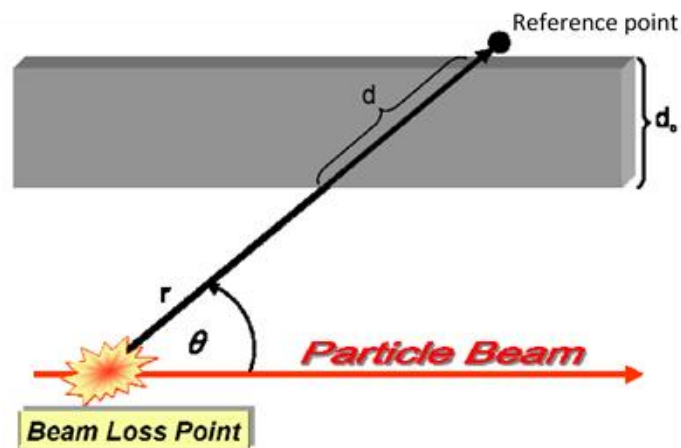


Figure 2.4 Application of the line-of-sight models to simple bulk shielding geometries

The dose (rate) at the reference point is derived from the source term H_0 and geometrical quantities. The dose $H(E_p, d, \theta)$ at the reference point can then be estimated as the Moyer model:

$$H(E_p, d, \theta) = H_0(E_p, \theta) \cdot \frac{1}{r^2} \cdot \exp\left(-\frac{d}{\lambda(\theta)}\right)$$

The Moyer model has been used in the shielding design of some proton therapy facilities; however, it is not appropriate for such use. There are many modified versions of the Moyer model which includes changes in attenuation length with shield thickness and includes a correction for oblique penetration through the shield.

For the Monte Carlo simulation method, many Monte Carlo codes are used extensively for shielding calculations. These codes can be used to do a full simulation, modeling the accelerator or beam line and the room geometry in its entirety. Monte Carlo computational models are independent of geometry typically consist of a source term and an exponential term that describes the attenuation of the radiation. Both the source term and the attenuation length are dependent on particle type and are a function of energy and angle and depend upon the composition and density of the shielding materials.

2.1.2 Secondary radiation: Neutron

There are many secondary radiations produced during primary proton slowing down and stopped. As proton are being delivered to the treatment room during the normal operation, there can be 1) beam losses along the beam line, 2) full beam incident on intentional targets such as beam stopper and 3) partial beam interception by device such as range shifter. All the above are broadly referred to as “beam losses”. Secondary radiation is produced in the patient and the dosimetric phantom.

2.1.2.1 Neutron classification

Neutrons are the elementary constituents of matter. It is bound with protons in nucleus by the nuclear force. The most concerning for shielding is neutron according to their lower interaction cross section, no coulomb interaction and difficult to detect. Depending on the neutron energy, low energy neutron, thermal neutron, has higher interaction cross section then it can be detected easier while high energy one cannot. High energy neutron lost their energy through many interactions, liberate lots of thermal neutrons which then be detected. The classification of neutron according to their energy range as illustrated in Table 2.2.

Table 2.2 Neutron energy classification

Neutron	Energy range
High energy	$E > 20 \text{ MeV}$
Fast	$100 \text{ keV} < E < 20 \text{ MeV}$
Intermediate	$1 \text{ eV} < E < 100 \text{ keV}$
Thermal	$0.01 \text{ eV} < E < 1 \text{ eV}$
Slow	Below 0.01 eV

2.1.2.2 Interaction of neutron with matter

Since neutrons are neutral in charge, they can travel significant distance in matter without undergoing interactions. Neutron collisions with atoms can result in elastic or inelastic reactions⁽¹²⁾. In an elastic reaction, the total kinetic energy of the incoming particle is conserved, whereas in an inelastic reaction, the nucleus absorbs some energy and is left in an excited state. Inelastic scattering can occur only at energies above the inelastic scattering threshold of the material. The possible interactions are illustrated in Figure 2.5.

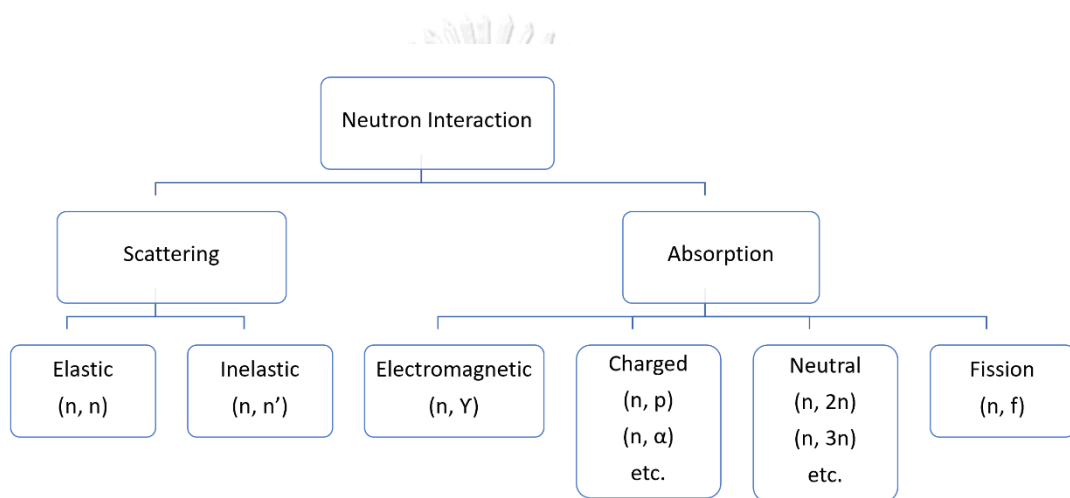


Figure 2.5 Categories of neutron interaction. The first letter in parenthesis shows the incoming and the second one for outgoing particles

In the other hand, the two major types of neutron interactions with matter are scattering and absorption. For scattering interaction, neutron transfers some kinetic energy to the nucleus. The neutron speed and direction change but the nucleus is left in the same state as before the interaction. If enough energy is transferred, the recoiling nucleus ionizes the material surrounding the interaction point.

For absorption interaction, the neutron interaction can cause the nuclear reaction. Instead of scattered by the nucleus, the neutron can be absorbed or captured. The products from the interaction such as protons, alpha particles, gamma rays and fission fragments can generate the detection process. Most of detection process take place at thermal neutron, except fast neutron for CR-39.

2.1.2.3 Neutron dosimetry

Neutron detection mechanism in matter is generally based on indirect methods. The neutron detection process begins when neutrons interacting with various nuclei and release one or more of charged particles such as protons. The electrical signals produced by the charged particles can be subsequently processed by the detection system.

2.1.3 Ambient dose equivalent

Following the definition of the ICRU report 51⁽¹³⁾, the ambient dose equivalent $H^*(10)$ at a point in a strongly penetrating radiation field is the dose equivalent that would be produced by the corresponding expanded and aligned field in the ICRU sphere at a depth of 10 mm on the radius vector opposing the direction of the aligned field. The ‘ICRU sphere’ is a theoretical phantom defined as “a 30 cm diameter tissue-equivalent sphere with a density of 1 g/cm³ and a mass composition of 76.2% oxygen, 11.1% carbon, 10.1% hydrogen and 2.6% nitrogen”. The ‘expanded and aligned field’ refers to a theoretical unidirectional field in which the fluence and its energy distribution are constant throughout the entire volume of interest (a 30 cm diameter sphere) and equal to the fluence and its energy distribution at the point of reference in the actual field. This concept is schematized in Figure 2.6.

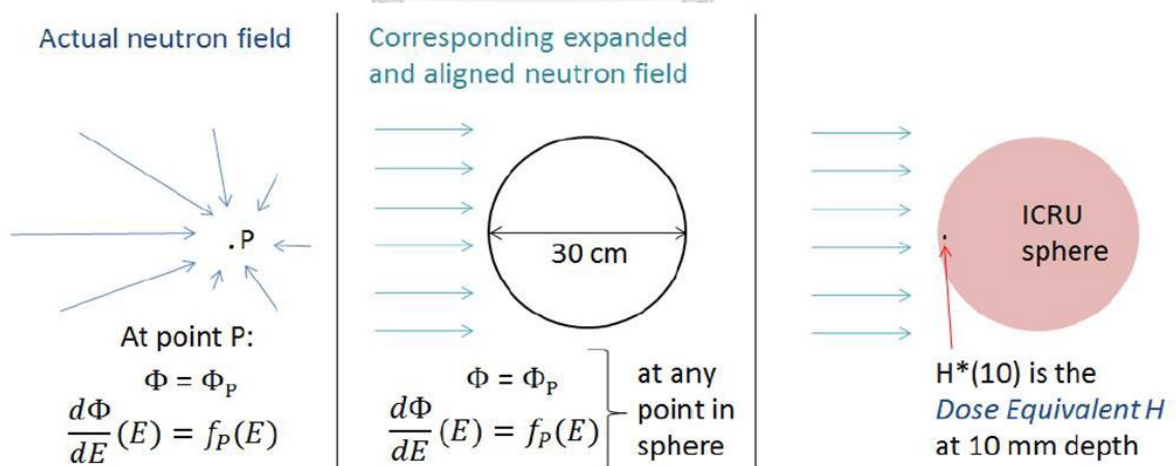


Figure 2.6 The concept of the ambient dose equivalent $H^*(10)$

When the neutron energy spectrum is identified (through calculation or measurement), the radiation protection quantities and the operational quantities can be calculated by unfolding that spectrum with the appropriate conversion coefficients recommended by the ICRP. The fluence-to- $H^*(10)$ conversion coefficients for neutrons from ICRP Publication 74⁽¹⁴⁾ (shown in Figure 2.7) are used to compute the neutron $H^*(10)$.

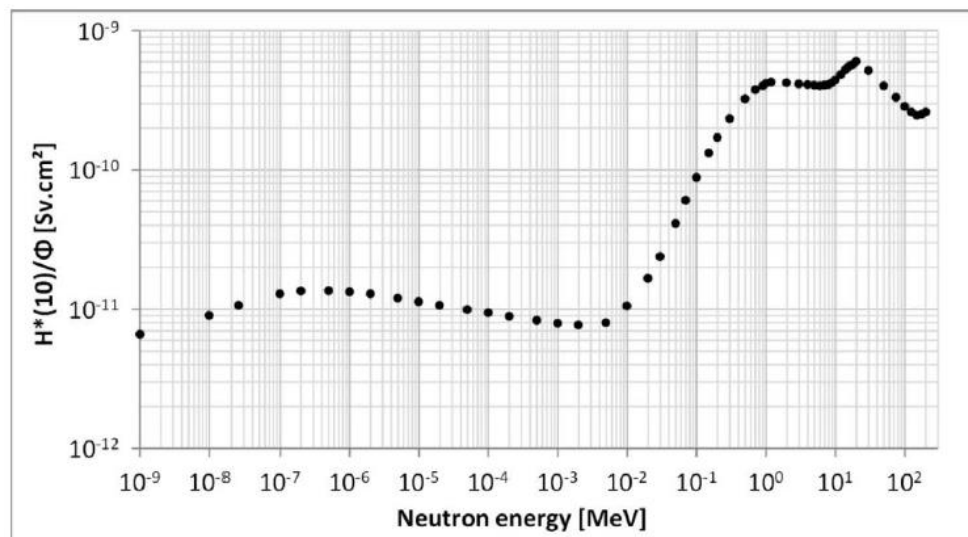


Figure 2.7 Fluence-to- $H^*(10)$ conversion coefficients (up to 200 MeV)

2.1.4 Neutron detection

Being neutrons uncharged particles, the detectors cannot detect them directly but can detect only the products of their interactions with matter. Almost all the detector type can be made sensitive to neutrons. Virtually every type of neutron detector involves the combination of a target material designed to carry out this conversion together with one of the conventional radiation detectors.

In general, neutron detectors can be divided into two main categories: neutron counters and neutron spectrometers. In the first case, the signal output does not depend on neutron energy. This kind of detector is most used for low-energy neutrons. Instead, for neutron spectrometers the signal depends on the neutron energy. To infer the neutron energy distribution the inversion procedure is used. Starting from

the measure of the energy of produced charged particles we try to obtain the neutron energy, through energy and momentum conservation law.

2.1.5 Polyallyl diglycol carbonate (PADC), CR-39

The passage of a charged particle through an inorganic or organic insulating material can damage the structure and create tracks. The polyallyl diglycol carbonate (PADC), $C_{12}H_{18}O_7$, plastic are the track etched detectors, as known as CR-39. Neutrons of a wide energy range are detected through nuclear reactions of $H(n,p)$ for thermal neutrons and $^{10}B(n,\alpha)^7Li$ on a converter for fast neutrons. The latent tracks, which was created by charged particles in the detector material, are magnified by etching. Figure 2.8 shows a typical neutron dosimeter element comprising PADC overlaid with a 1 mm thick polyethylene radiator. Recoil proton tracks can originate in the radiator itself, or within the body of the PADC. Tracks are revealed if part of their path length is within the etched volume of the plastic, i.e., the volume between the pre- and post-etch surfaces.

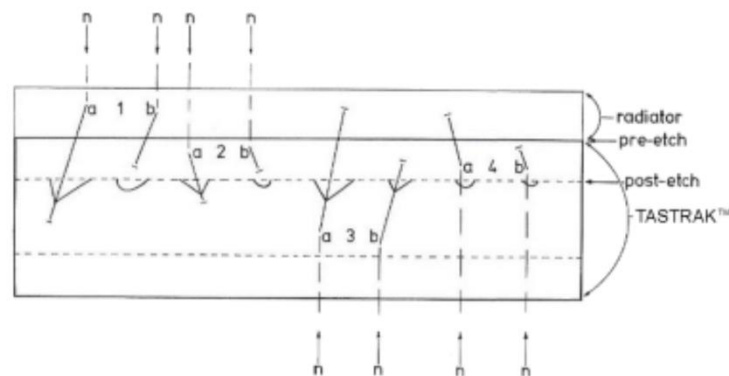


Figure 2.8 Miscellany of recoil proton tracks

The track parameters enable to calculate so-called etch ratio V of every track according to following equation

$$V = \frac{V_T}{V_B}$$

where V_T is etched rate of damaged material in area of particle path,

and V_B is etched rate of unaffected detector material.

There are the study of the variation of etching method⁽¹⁵⁾ from the standard etching conditions ,Etching: 2 h and 50 min at 85°C in 6.25 N NaOH. It demonstrated that the variation of etching duration and etching temperature does not have a significant influence on the measured doses of detectors, the variation of calculated neutron doses is within 20 %.

However, the influence of the etching temperature on the sensitivity of irradiated detectors is not negligible: a decrease of 5 % per 1°C increasing temperature could be observed. The study indicated that the recommended etching procedure of 2 h 50 minute at 85°C is applicable for routine applications.

2.1.6 Neutron moderator types

The aim of using neutron moderator is to reduce or moderate the energy (speed) of the neutron in the sample region or the detector region. The idea of moderating is to use materials with nuclear properties such as a large scattering cross-section, small absorption (capture) cross-section and large energy loss per collision. Neutron attenuation is accomplished by elastic and inelastic scattering reactions which reduced the neutron energy until the capture is possible. The neutron cross-sections of the most common isotopes are shown in Table 2.3.

Table 2.3 The example of neutron cross-sections

		Thermal neutron			Fast neutron		
		Scattering	Capture	Fission	Scattering	Capture	Fission
Moderator	H-1	20	0.2	-	4	0.00004	-
	H-2	4	0.0003	-	3	0.000007	-
	C-12	5	0.002	-	2	0.00001	-
Structural materials, others	Zr-90	5	0.006	-	5	0.006	-
	Fe-56	10	2	-	20	0.003	-
	Cr-52	3	0.5	-	3	0.002	-
	Ni-58	20	3	-	3	0.008	-
	O-16	4	0.0001	-	3	0.00000003	-
Absorber	B-10	2	200	-	2	0.4	-
	Cd-113	100	30	-	4	0.05	-
	Xe-135	400	2,000,000	-	5	0.0008	-
	In-115	2	100	-	4	0.02	-

The neutron cross-section is variable and depends on; 1) Target nucleus (hydrogen, boron, uranium, etc.) Each isotope has its own set of cross-sections. 2) Type of the reaction (capture, fission, etc.). Cross-sections are different for each nuclear reaction. And 3) Neutron energy (thermal neutron, resonance neutron, fast neutron). For a given target and reaction type, the cross-section is strongly dependent on the neutron energy. In the common case, the cross-section is usually much larger at thermal neutron energies.

2.2 Literature review

Fehrenbacher et al.^(4, 5) studied the response of a new neutron dosimeter which was developed for the measurement of high-energy neutron radiation. The lead (Pb) layer was added inside the polyethylene (PE) sphere around Thermoluminescence detection (TLD) elements (pairs of TLD 600/700). The response function of the GSI ball was simulated using FLUKA and MCNP Monte Carlo code. An averaged curve from both simulations is computed and displayed in Figure 10 (Left). The measurement of the dosimeter response was performed at the accelerator facility of the PTB in Braunschweig and the Geesthacht Neutron Facility (GeNF) laboratory at the GKSS research center. The measured fluence responses are 27% too low for thermal energies and show an agreement with ~14% for the accelerator produced neutron fields related to the computed fluence responses, as shown in Figure 2.9 (Right).

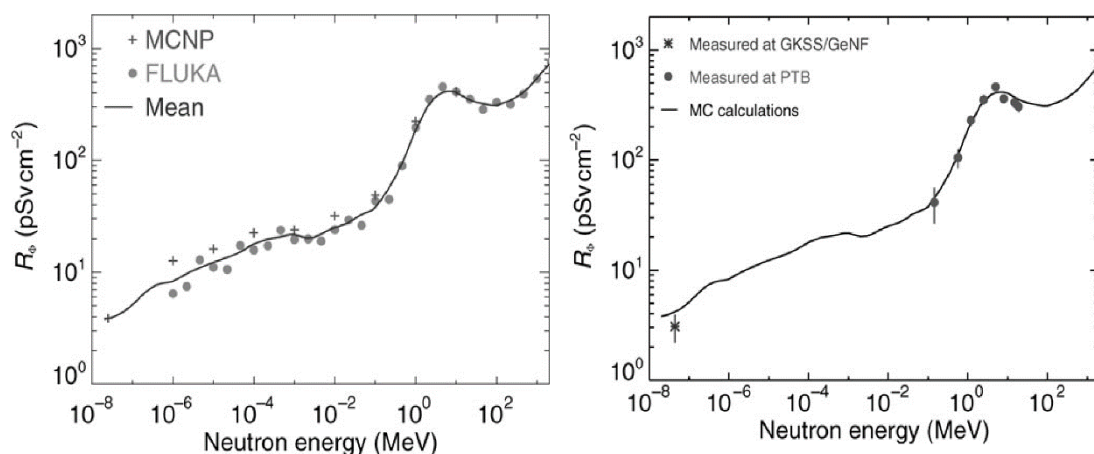


Figure 2.9 An averaged calculated response function, solid line, from FLUKA and MCNP.

Sokolov et al.⁽³⁾ studied on the passive neutron detector for area monitoring at high-energy accelerators. With the objective of finding a dosimeter that fulfils the necessary requirements and can be reliably used to prove that the radiation levels in areas around accelerators are in accordance with the limits of the respective radiation protection. A simple layout with small dimensions and light weight as well as the usage of common materials to lower the production costs was used in this study. In comparison with the currently used passive dosimeter at GSI, the layouts are simplified, and the weight is reduced. The design of the dosimeter and its applicability for radiation survey are investigated using the FLUKA Monte Carlo simulation code, as shown in Figure 2.10.

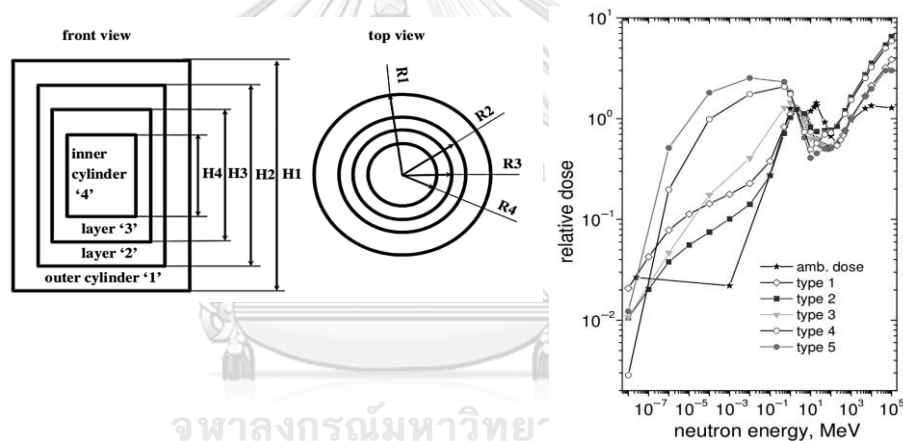


Figure 2.10 The layout of the dosimeters and the simulated response function

Satoh et al.⁽¹⁶⁾ reported the neutron ambient dose equivalent behind the concrete shields and at the maze which measured with three detectors (DARWIN, Wendi-2, and a rem meter) along with solid-state nuclear track detectors. The measured data were compared with estimations of analytical models and the Monte Carlo simulation, Particle and Heavy-Ion Transport code System (PHITS). The analytical model, using the parameters employed in the shielding design of the facility, gave larger values than the measured data. This means that the facility was designed with a sufficient margin of safety. The results calculated by PHITS were less than those of the analytical model and were about three times larger than the measured data. Among these three detectors, the lack of sensitivity to high-energy neutrons, below 17 MeV,

of the rem meter caused underestimate the $H^*(10)$ rate about 2.5 times when compared to DARWIN and Wendi-2 detectors. According to the energy spectra measured by DARWIN, the effective dose is about 40% less than the ambient dose equivalent under the present experimental conditions.

Trinkl et al.⁽¹⁷⁾ measured the neutron fluence energy distributions with an extended-range Bonner sphere spectrometer featuring ^3He proportional counters at 2 meters from the isocenter. A Bonner sphere spectrometer consists of several polyethylene spheres which each size was designed for neutron energy. At the same location, the ^3He proportional counters with various the PE sphere sizes has been used to detect the fluence of the neutrons. All the measured data were unfolded to get the neutron spectrum at the point. The neutron spectrum was then multiplied with the fluence-to-ambient dose equivalent conversion factor. When compared the mono energetic proton plans of 75 MeV and 200 MeV, the increasing of $H^*(10)$ was about a factor of 50. The existence of a peak of secondary neutrons in the MeV region was demonstrated in beam direction (position 1). The experiment setup and the details of the plans are demonstrated in Figure 2.11.

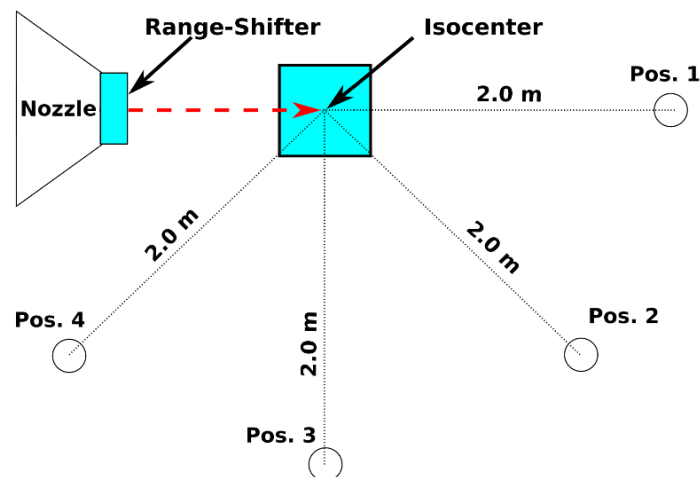


Figure 2.11 The schema of experimental setup at RPTC

The using single mono-energetic layers ($11 * 11 \text{ cm}^2$) within a $30 * 30 * 30 \text{ cm}^3$ PMMA phantom, and primary proton energies of 75, 140 or 200 MeV. The range shifter for the irradiation with 118 MeV protons was placed at the end of the nozzle.

Positions 1–4 showed the measurement positions with the Bonner sphere spectrometer.

A strong angular and energy dependence of the secondary neutron field within the treatment room was found. They recommended that the simulation of the secondary neutrons within a proton treatment room must include geometric features of the spatial characteristics of the area surrounding the isocenter of the irradiation and corresponding construction materials (e.g., room walls, Gantry wheel, counterweight)



CHAPTER 3 RESEARCH METHODOLOGY

The detection of the operational quantity: ambient dose equivalent, $H^*(10)$ will lead to the considering of the radiation area monitoring in proton therapy. With only one WENDI-II system, it might take long time to get the $H^*(10)$ in various location. It is encouraging our motivation to create the new neutron moderator detectors to shorten the area monitoring understanding.

3.1 Research question

What is the performance of the new moderated neutron detector for the determination of the accumulated ambient dose equivalent, $H^*(10)$, in proton therapy?

3.2 Research objective

To validate the new moderated neutron detector for the determination of the accumulated ambient dose equivalent, $H^*(10)$, in proton therapy.

3.3 Research design

Cross-sectional Observational descriptive study

3.4 Conceptual framework

The ambient dose equivalent is affected by several factors, such as the Traceability and the calibration process, the detection efficiency of the detector and the measurement conditions. The conceptual framework is shown in Figure 3.1.

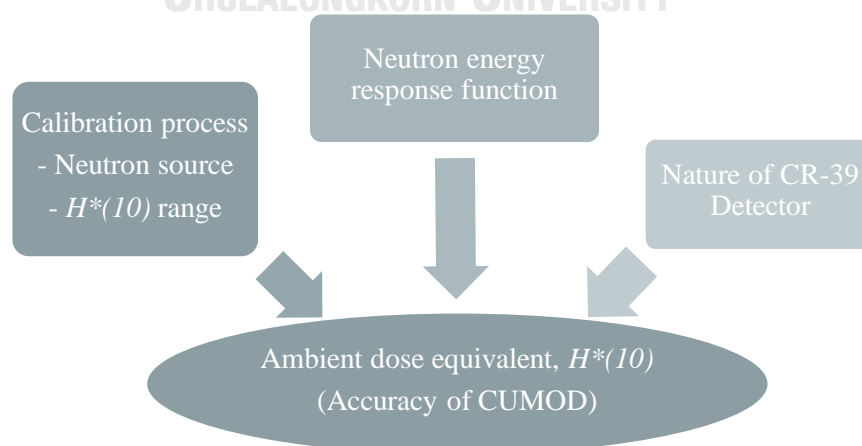


Figure 3.1 The conceptual framework

3.5 Research design model

The research design model is described in Figure 3.2 where the study started with the design and the creation of the CUMOD. The calibration factor received through the detector calibration. The measurement of ambient dose equivalent from CUMOD was compared with the ambient dose equivalent dose from WENDI-II.

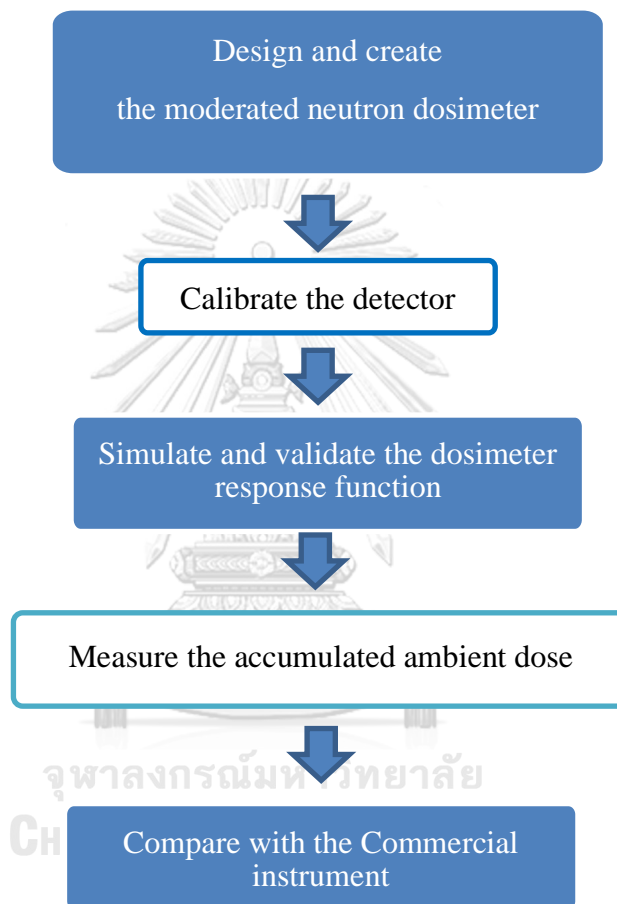


Figure 3.2 The research design model

3.6 Expected benefit

CUMOD can be used for Ambient dose equivalent measurement with confidence. The using of CUMOD for accumulated ambient dose equivalent measured in various locations, in addition to WENDI-II, can shorten the understanding of the radiation area monitoring in proton therapy.

3.7 Variable measurement

The Independent variables are the proton plans, the medium used as the target and the measured distance and location.

The dependent variable is the ambient dose equivalent from CUMOD.

3.8 Data collection

The ambient dose equivalent from CUMOD detectors were collected and compared to Wendi-II detector.

3.9 Data analysis

The ratio of ambient dose equivalent of CUMOD and WENDI-II was plotted to evaluate the response of CUMOD.

The relationship between CUMOD and WENDI-II were investigated to validate the use of CUMOD as area monitoring.

3.10 Outcome

The outcome of this study is the ambient dose equivalent from CUMOD.

3.11 Statistical analysis

Descriptive statistics: maximum, minimum, mean, and standard deviation were used for analysis using the Microsoft Excel program. The percentage difference will be used to compare the amount of ambient dose equivalent from CUMOD and WENDI-II

3.12 Ethical consideration

According to the ethical consideration, this study respects for person authority, the principle of beneficence/non-maleficence, and justice rule. This study was performed in a solid water phantom. The research proposal has been submitted to the Ethics Committee of Faculty of Medicine, Chulalongkorn University, Bangkok, Thailand, for approval. The certificate of approval from the Institutional Review Board (IRB) is demonstrated in Figure 3.3.

CHAPTER 4 MATERIALS AND METHODS

The CUMOD was designed to measure the ambient dose equivalent in compact proton therapy with the proton energy up to 220 MeV. The CR-39 was selected as the measurement detector. The materials and methods are described below.

4.1 Materials

4.1.1 ProBeam® compact single-room proton therapy

The ProBeam Compact single-room proton therapy (Varian Medical System, Palo Alto, CA) has the pencil beam spot scanning treatment nozzle which allowed the utilizing of Intensity Modulated Proton Therapy (IMPT). The clinical interested beam parameters are shown in Table 4.1.

Table 4.1 The interested clinical beam parameters

Parameter	Typical Value
Energy	69 – 220 MeV $\pm 2\%$
Tunable range (w/o range shifter)	4.0 – 30.0 g/cm ² (in water)
Maximum field size	30 × 40 cm ²

The proton therapy center at Her Royal Highness Princess Maha Chakri Sirindhorn Proton Center, King Chulalongkorn Memorial Hospital is three stories building. Most parts of the building are in the underground. The minimum thickness of the shielding is about 2 meters. The layout of this proton center is revealed in Figure 4.1.

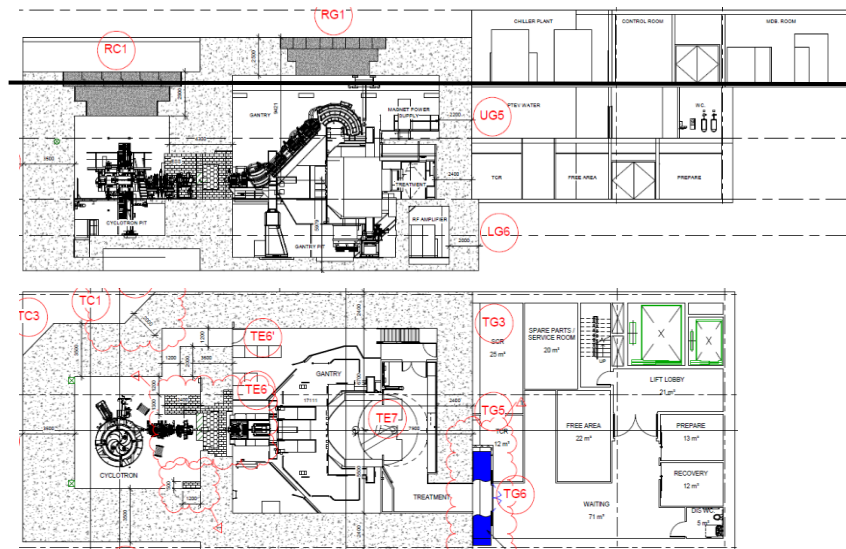


Figure 4.1 The layout of our center. Building section (Top). Treatment floor (Bottom)

4.1.2 Neutron sources

The ^{241}Am -Beryllium neutron calibrator source OB 26/8501 (Buchler, Braunschweig, West-Germany), at the Office of Atom for Peace (OAP), Bangkok, Thailand was used in this study. The source was received in 1981 from International Atomic Energy Agency (IAEA) with the activity of 185 GBq. The ambient dose equivalent rate was $115 \mu\text{Sv/hr}$ at 1 meter. The air scattering factor and room scatter factors lie in between 1.004 to 1.018, and 1.004 to 1.044 at a distance from 0.595 m to 2.0 m, respectively⁽¹⁸⁾. The calibrator source and the schematic are shown in Figure 4.2.

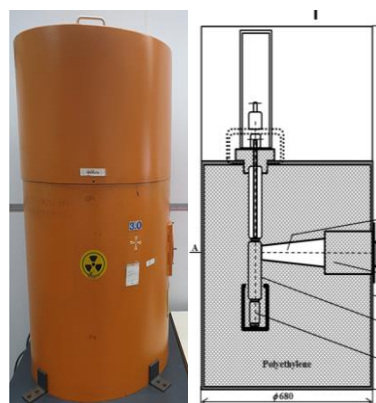


Figure 4.2 The $^{241}\text{AmBe}$ calibrator source and the schematic

4.1.3 Wide-Energy Neutron Detection Instrument (WENDI-2)

The Wide-Energy Neutron Detector, WENDI-II (Thermo Fisher Scientific, Waltham, MA) has been widely used to measure the $H^*(10)$ both inside and outside the proton treatment room⁽¹⁹⁻²¹⁾. More than the convenience, the reliable $H^*(10)$ results are the key to use this active detector.

The WENDI-2 is a cylindrical neutron rem meter developed in the 1990s that has an extended energy range from thermal energies to 5 GeV. This rem meter has four main components: a cylindrical polyethylene moderator, tungsten powder shell, borated rubber patch, and cylindrical ^3He proportional counter. In the center of this instrument, a cylindrical ^3He (pressurized at 2 atm.) proportional counter detects thermal neutrons (using (n, p) reaction) that passed through the moderator with tungsten powder shell and borated patch, as shown in Figure 4.3.

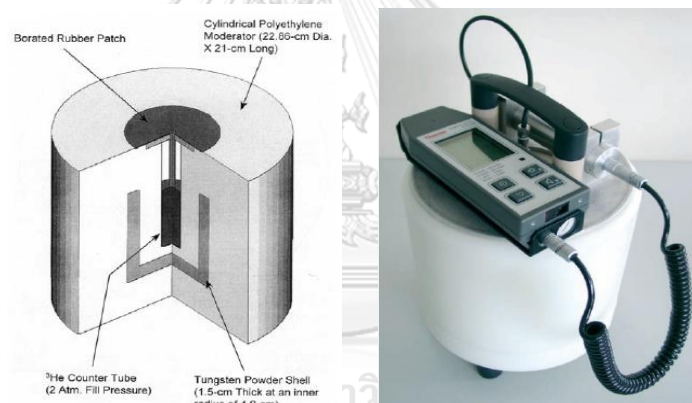


Figure 4.3 Cutaway view of the WENDI-2 and WENDI-2 connected to a survey meter

The non-statistical uncertainties from WENDI-2 measurement are from the difference between the response function of WENDI-2 and fluence-to dose conversion coefficients from ICRP 74. The WENDI-2 was calibrated using ^{252}Cf source, which is a neutron source with an energy range from 0.1 to 15 MeV. Due to the response function of WENDI-2, it underestimates in the energy range from 5 to 100 MeV and overestimates below 0.1 MeV and above 100 MeV. The previous literature about neutron dose measurement in the proton therapy facilities reported the uncertainties around 20%⁽²²⁾.

4.1.4 CR-39

The Poly Allyl Diglycol Carbonate (PADC), commonly known as CR-39 (Track Analysis System Ltd, Bristol, UK), is a dosimetry grade plastic with the ability to record tracks of electrically charged nuclear particles. An important property of TASTRAK™ PADC is that it is highly selective in its recording of nuclear tracks. Thus, the plastic is insensitive to visible light and does not record x-rays, gamma-rays or tracks of beta-particle electrons but is highly effective in the recording of alpha-particles at natural energies, protons with energies up to around 9 MeV, heavy ions and fast ions generated in laser-plasma interactions.

With the size of $2 \times 2.5 \times 0.1 \text{ cm}^3$, the clear plastic plate, density of 1.3 g/cm^3 , responds to the neutron energy of 200 keV -14 MeV. This CR-39 can measure the ambient dose equivalent in the dose range of $100 \mu\text{Sv} - 600\text{mSv}$ with the sensitivity of 150 to 750 tracks/mSv which depend on the calibration process. The CR-39 was served as the whole plate, shown in Figure 4.4. After cutting for piece, The CR-39 was ready to use.



Figure 4.4 The whole plate and after cutting of CR-39

4.1.5 Etching water bath

The water bath, Figure 4.5 (Right), used to etch the CR-39. The inner dimensions are large enough to contain the etch and scanning frame, Figure 4.5 (Left). The constant temperature of 85°C for 2 hours 50 minutes was utilized for the NaOH solution.

4.1.6 TASLIMAGE automatic reader system

The TASLIMAGE system is based on a microscope (high-quality Nikon optics) and an ultra-fast three-axis motorized control for scanning the detectors, as shown in Figure 4.6. With the ultrafast scanning speed of $10 \text{ mm}^2/\text{s}$, the read-out time of each CR-39 for the area of 1 cm^2 is about 40 s. For 49 CR-39 per scanning frame, the total read-out time is about 35 minutes (repeat 3 times for each CR-39).



Figure 4.5 The water bath (Right) and the etch and scanning frame (Left)



Figure 4.6 TASLIMAGE automatic reader system

Etch-tracks from recoil protons are typically 3-15 microns in size. The track sizes overlap with those for alpha-particles at large track sizes, where shape differences are used to discriminate particle species. At the small track sizes, efficient discrimination between noise (primarily dust on the surface) and genuine tracks is achieved with the measurement of 26 track parameters, including a variety of size and shape characterizations. These allow discrimination of tracks against high backgrounds of non-track features per cm^2 without compromising the measurement accuracy. Even a low energy fast neutron signal ($\sim 200 \text{ keV}$), which is almost identical

to that of the background, is distinguishable by use of a variety of complex shape-detection algorithms.

4.1.7 Moderator materials

There were 2 types of moderator materials used in this study, the 5% borated polyethylene and Cerrobend alloy.

The 5% borated polyethylene (Marshield, Ontario, Canada) is boron filled polyethylene usually used to attenuate and absorb neutron. The borated polyethylene contains 5% boron content by weight has the density of 1.04 g/cm^3 . The standard sheet size is $48 * 96 * 1 \text{ inch}^3$, as shown in Figure 4.7 (Right) The composition of Boron in $(\text{C}_2\text{H}_4)_n$ allowed us to reduce the moderator size compared to other neutron detectors.

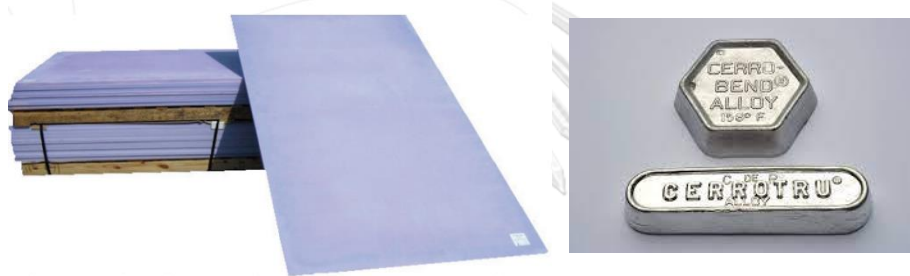


Figure 4.7 The 5% borated polyethylene (Right) and Cerrobend alloy (Left)

The Cerrobend alloy used in radiotherapy in the purpose of making the photon customized block, as shown in Figure 4.7 (Left). With the melting point of 70°C , the Cerrobend alloy can easily form the shape we designed. The composition of 50% Bismuth, 26.7% Lead, 13.3% Tin and 10% Cadmium, with the density of 9.38 g/cm^3 is the challenge in terms of neutron scattering. The purpose of selecting Cerrobend is to reduce the energy of high energy neutron.

4.1.8 Solid water phantom

Solid water phantom RMI 457 (GAMMEX RMI, WI, USA) possess normal density and average atomic number of 1.03 g/cm^3 and 5.96, respectively. The dimensions is $30 * 30 \text{ cm}^2$, with a standard range of thicknesses from 0.2 to 5.0 cm. The total thickness of 35 cm was used to stop all the proton beam and then the

neutron was generated from this phantom. The orientation of the phantom thickness was according to the direction of the proton plans, as shown in Figure 4.8.

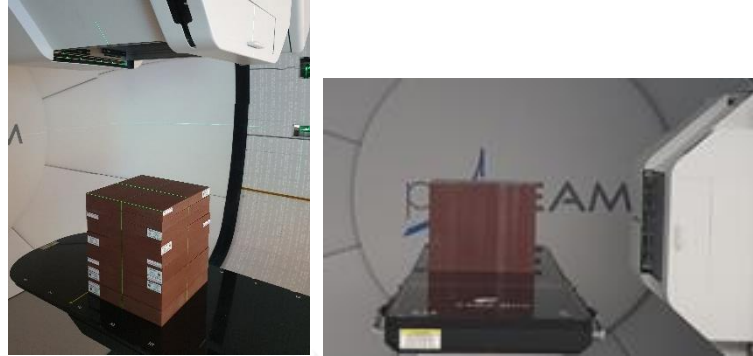


Figure 4.8 The solid water phantom and its orientation according to the proton plans

4.1.9 PHITS monte carlo code

PHITS (Particle and Heavy Ion Transport code System) is a general purpose Monte Carlo particle transport simulation code developed under collaboration between JAEA, RIST, KEK and several other institutes. It can deal with the transport of all particles over wide energy ranges, using several nuclear reaction models and nuclear data libraries. The recommend models are shown in Figure 4.9. PHITS can support the researches in the fields of accelerator technology, radiotherapy, space radiation, and in many other fields which are related to particle and heavy ion transport phenomena. The version of 3.22 was used in this study.

	Neutron	Proton, Pion (other hadrons)	Nucleus	Muon	e^- / e^+	Photon
High ↑ Energy ↓ Low	1 TeV	1 TeV/u				1 TeV
	Intra-nuclear cascade (JAM) + Evaporation (GEM) 3.0 GeV	JAMQMD + GEM	Virtual Photo-Nuclear JAM/ JQMD + GEM 200 MeV	EGS5 or Track structure	EGS5 or EPDL97	Photo-Nuclear JAM/ JQMD + GEM + JENDL + NRF
	Intra-nuclear cascade (INCL4.6) + Evaporation (GEM) 20 MeV	d t ³ He α 10 MeV/u	Quantum Molecular Dynamics (JQMD) + GEM			
	Nuclear Data Library (JENDL-4.0) + (EGM) 0.01 meV	1 MeV	Energy loss by ATIMA or track structure	ATIMA + Original	1 keV	1 keV
	1 keV		Muonic atom + Capture	Track structure 1 meV		

Physics models of PHITS and their switching energies

Figure 4.9 Map of models recommended to use in PHITS

4.2 Methods

The following steps were performed to conduct this research, including CUMOD design and creation, MC simulation for CUMOD response function, CUMOD calibration and determination of the ambient dose equivalent.

4.2.1 Design and create the moderated neutron dosimeter

The cylindrical shape of the neutron detector was designed and demonstrated in Figure 4.10. The cylindrical 5% Borated polyethylene, 10 cm diameter * 10 cm height was inserted with the Cerrobend alloy 1.5 cm thick at an inner radius of 5 cm. The total of 4 pieces of CR-39 were equipped inside the CUMOD

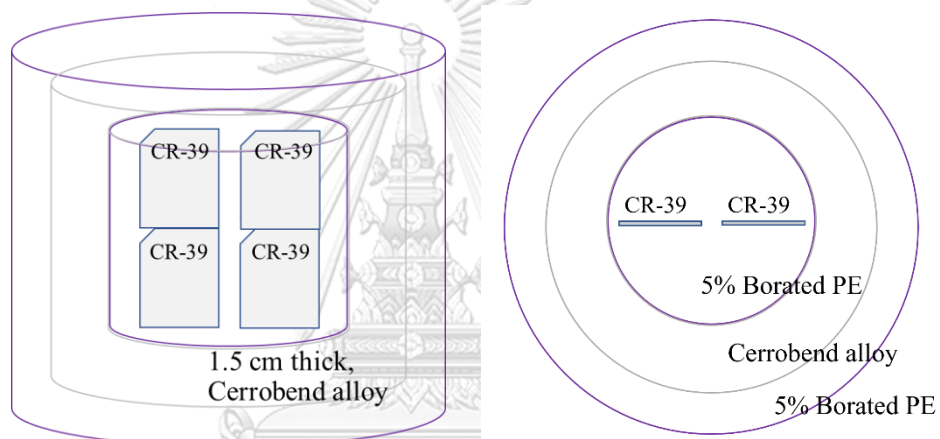


Figure 4.10 The design of CUMOD side view(left) and top view (right)

4.2.2 Calibration of CUMOD neutron detector

The CUMOD was calibrated with $^{241}\text{AmBe}$ source calibrator at the Office of Atom for Peace (OAP), Bangkok, Thailand. According to the $H^*(10)$ rate of $115 \mu\text{Sv/hr}$ and the availability of the OAP laboratory, CUMOD was calibrated in the range of $100 \mu\text{Sv}$ to $2,000 \mu\text{Sv}$. The CUMOD was placed at 100 cm away from the neutron source, as shown in Figure 4.11. To get the desired $H^*(10)$, The irradiation time was in the range of about 50 mins to 18 hrs.



Figure 4.11 The calibration of CUMOD at 100 cm from the $^{241}\text{AmBe}$ calibrator source

4.2.3 Simulation of CUMOD response function

The details of size and atomic composition of CUMOD and CR-39 were expressed to PHITS MC, APPENDIX I. The tally mode of dose deposit was selected for all 4 CR-39s. The parallel neutron source was created on one side of CUMOD. The number of initiatives neutron was preferred to less than 5% error of the tally results. The neutron energy was varied from 1 meV to 1 GeV.

4.2.4 Validation of CUMOD response function

The validation of CUMOD response function could be performed in the same manner as a GSI ball⁽⁴⁾ where the mono-energetic neutron beams were used to validate the response of each neutron energy. Unfortunately, with the limitation of the neutron beam in our country, the known neutron spectrum beams from a few previous studies were used instead. As the new moderated neutron detector, CUMOD response function was validated together with WENDI-II for comparison.

For the neutron energy range of 10 eV to 15 MeV, Howell et al.⁽²³⁾ has reported the $H^*(10)$ of 1.1 $\mu\text{Sv}/\text{MU}$ with the setup of closed jaw X, Y and multileaf collimator at 40 cm away from the isocenter form Varian Clinac 21EX (Varian Medical System, Palo Alto, CA) . The schematic diagram and the neutron spectrum are shown in Figure 4.12. The setup was adjusted to make WENDI-II possibly measured. The

gantry was rotated to 270 degree position and the measurements at 40 cm from isocenter were performed for CUMOD and WENDI-II, as shown in Figure 4.13.

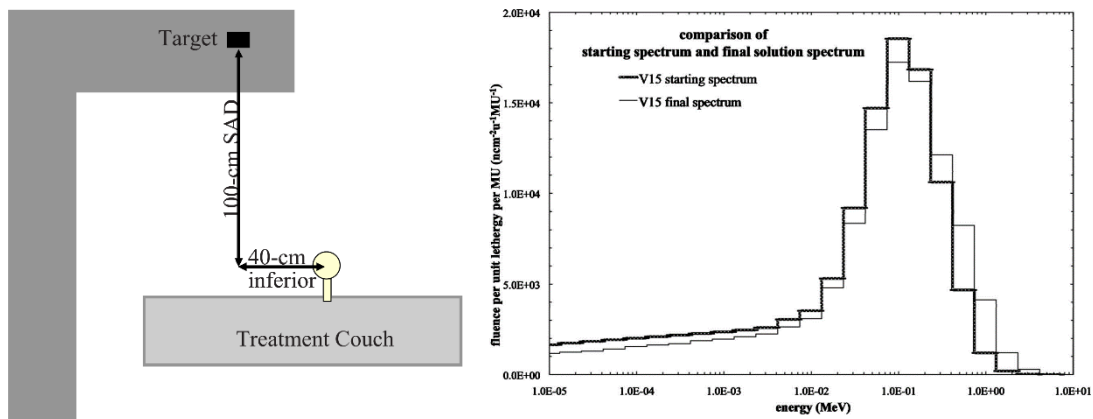


Figure 4.12 Schematic diagram of the measurement location and the 15 MeV linac neutron spectrum



Figure 4.13 The measurement of $H^*(10)$ of CUMOD and WENDI-II at Varian clinac 23EX for fast neutron response function validation.

For the high energy neutron, Trinkl et al.⁽¹⁷⁾ has reported the neutron spectrum for pencil beam scanning technique with the field size of $11 * 11 \text{ cm}^2$ on $30 * 30 * 35 \text{ cm}^3$ solid water phantom at the distance of 2 m from the isocenter. We selected the measured position of 45 degree instead of 0 degree, which has the highest $H^*(10)$, because of the limitation of the 2 m distance. The energy of 140 MeV and 200 MeV were selected with the $H^*(10)$ report of $3.2 \mu\text{Sv/Gy}$ and $11 \mu\text{Sv/Gy}$, respectively. The

neutron spectrums are shown in Figure 4.14. The CUMOD and WENDI-II were measured at 45 degree and 2 m to isocenter, as shown in Figure 4.15.

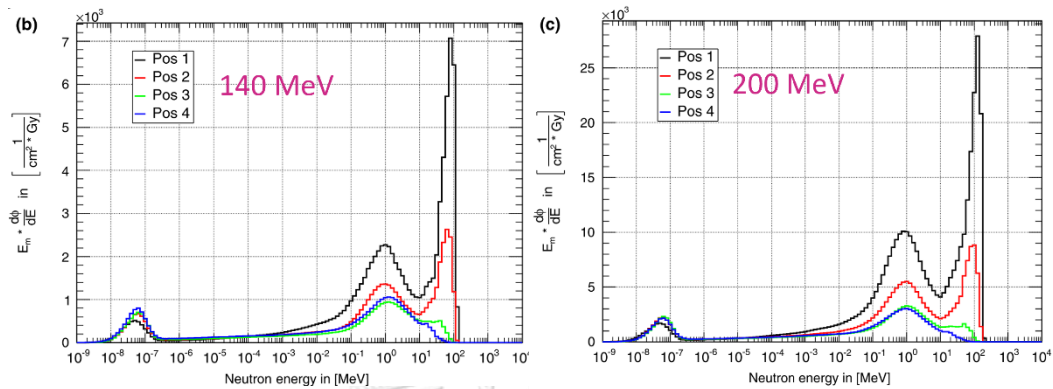


Figure 4.14 The neutron spectrum of 140 MeV and 200 MeV, the red line presents the 45 degree measurements.



Figure 4.15 The measurement of $H^*(10)$ of CUMOD and WENDI-II at proton therapy for high energy neutron response function validation.

4.2.5 Ambient dose equivalent measurements

The ambient dose equivalent, $H^*(10)$, inside the proton treatment room was measured first by WENDI-II. With the expected $H^*(10)$ larger than $100 \mu\text{Sv}$, as the minimum detectably of the CUMOD, the measurement using CUMOD was went along.

The measurement of $H^*(10)$ were performed at the zero degree to the neutron source. The solid water phantom, $30 * 30 * 35 \text{ cm}^3$ was laid on the treatment couch and the surface at the isocenter. The WENDI-II was positioned 100 cm away from

isocenter and CUMOD was employed at the same position, shown in Figure 4.16. The field size of $10 * 10 \text{ cm}^2$ proton plans were created using the beam scanning technique from Eclipse treatment planning system version 16.1.0 (Varian medical system, Palo Alto, CA).

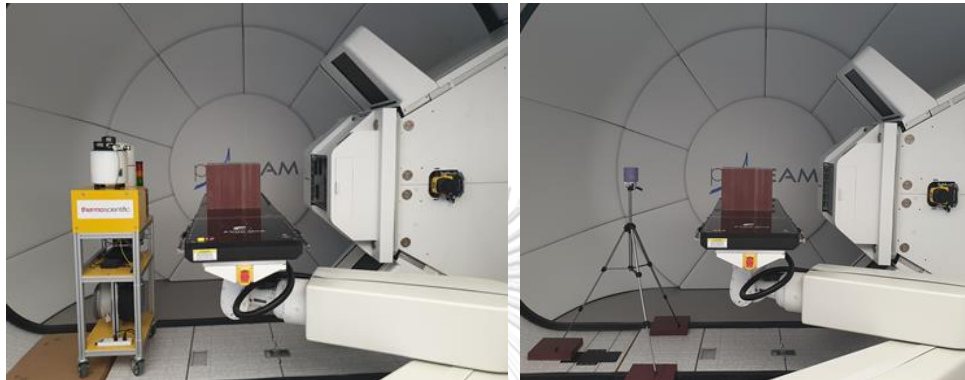


Figure 4.16 The ambient dose equivalent measurement setup at 0 degree at 100 cm distance from isocenter, Wendi-II (Right) and CUMOD (Left)

The plans were separated into 2 scenarios. For the first scenario, the single energy dose plane at the depth of 10, 20 and 30 cm were created with the expected of less neutron energy spreading. Then the multiple energy volume depth of 10, 20 and 30 cm were created with the expected of less neutron energy spreading. Then the multiple energy volume dose of $10 * 10 * 10 \text{ cm}^3$ at the same as previous depths, were generated for the broad neutron energy range. For the volume dose of depth 10 cm, the 5 cm range shifter was employed to get the full dose coverage to the surface. The dose distribution of all plans is illustrated in Figure 4.17.

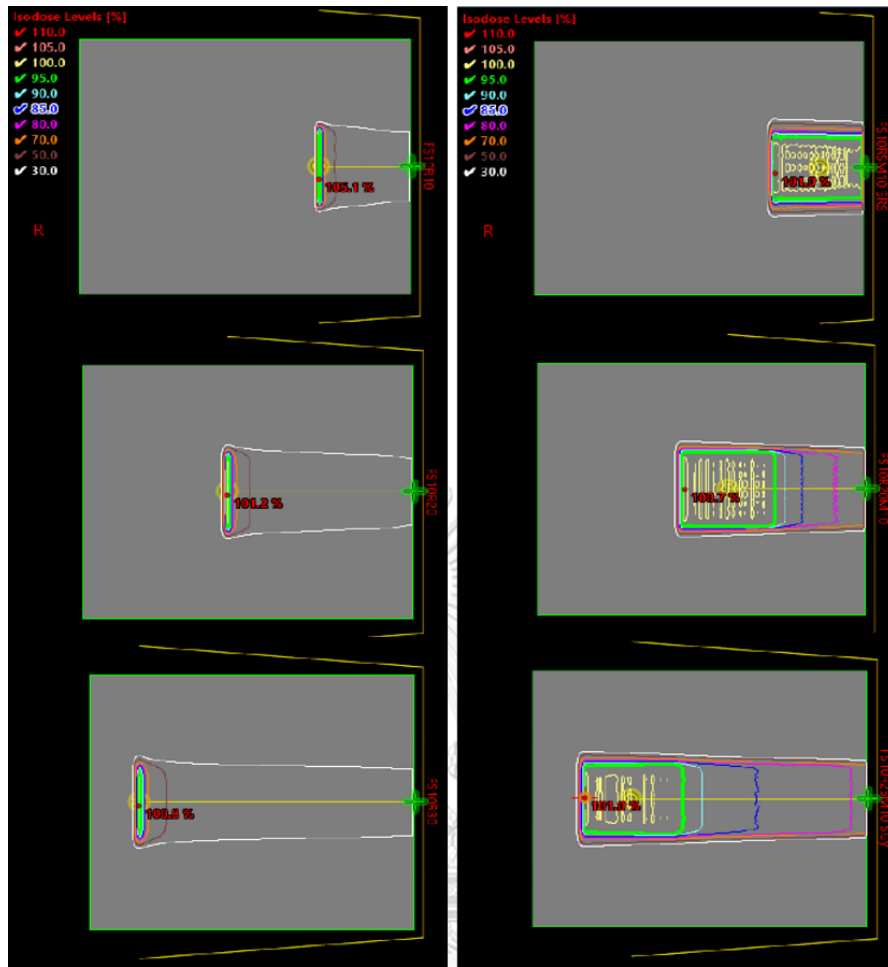


Figure 4.17 The dose distribution of plane dose (left) and volume dose (right)

CHAPTER 5 RESULTS

5.1 Design and create the moderated neutron dosimeter

The cylindrical shape of the neutron detector was created. The 5% borated polyethylene, the Cerrobend alloy and 4 pieces of CR-39. was constructed as CUMOD, as shown in Figure 5.1.



Figure 5.1 The Chulalongkorn University Neutron Moderator (CUMOD)

5.2 Calibration of CUMOD

The CUMOD was calibrated with $^{241}\text{AmBe}$ source calibrator at the Office of Atom for Peace, Bangkok, Thailand. After neutron irradiation, all CR-39 were etched in 6.25 N NaOH at 85°C solution for 2 h and 50 min then read by automatic reading system for 3 times per each CR-39. The characteristics of the particle track were illustrated in Figure 5.2. The number of tracks increases with the increasing of $H^*(10)$. The results are presented in Table 5.1. The 2000 μSv data was excluded from the calibration curve on the assumption that the source was sooner draw back in the safe.

Table 5.1 The $H^*(10)$ and no. of tracks in the CUMOD calibration process

$H^*(10)$: μSv	Tracks	SD	Track-B/G
100	125	85	92
300	304	118	271
500	475	126	442
1000	726	301	693
2000	729	76	696
B/G	33	9	

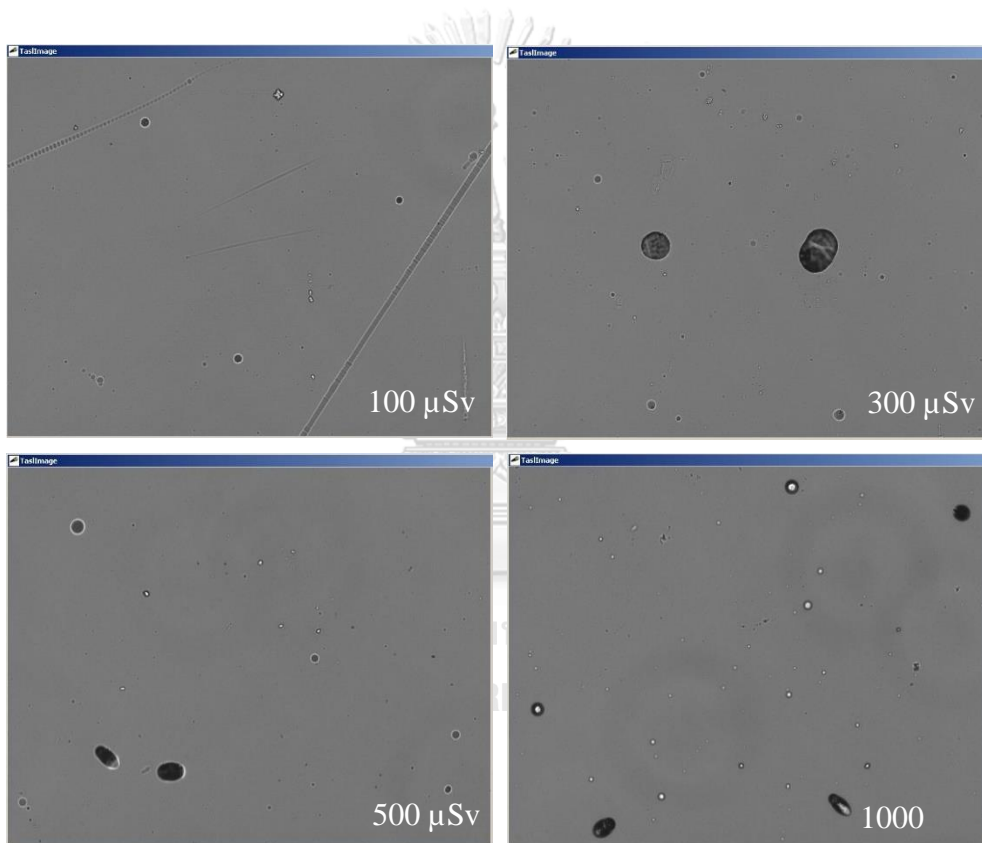


Figure 5.2 The characteristic of the particle tracks from different $H^*(10)$

The calibration factor, to converse number of tracks to $H^*(10)$, was 0.7441. The curve between number of tracks and $H^*(10)$ are plotted in Figure 5.3. The linear relationship with $R^2 = 0.9867$ was observed.

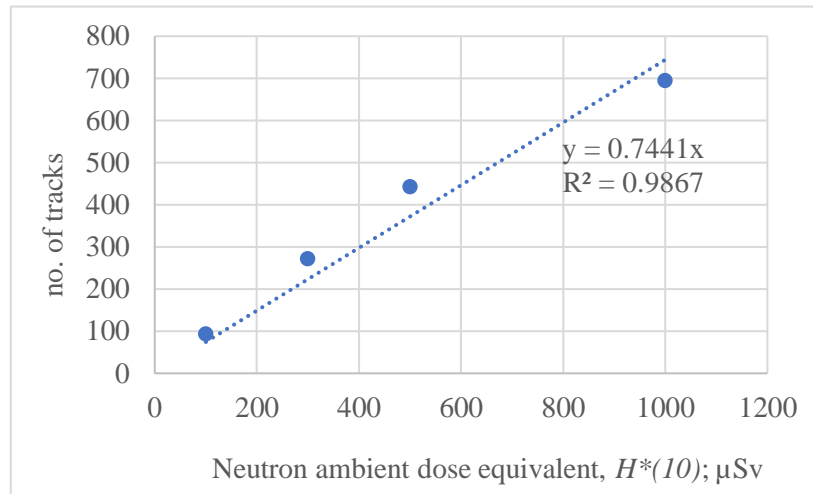


Figure 5.3 The linear relationship between number of tracks and $H^*(10)$

5.3 Simulation of CUMOD response function

With PHITS monte carlo simulation, after input the data, the geometry was inspected and displayed in Figure 5.4. The different colors represented the different materials. The T-deposit tally mode was used to compute the deposited energy ($\text{MeV}/\text{cm}^3/\text{source}$) in the interesting regions. For our simulation, the 4 pieces of CR-39 are the scoring regions. The average results are shown in Table 6. The number of initiated neutrons which was enough to keep the relative error lower than 5% were collected.

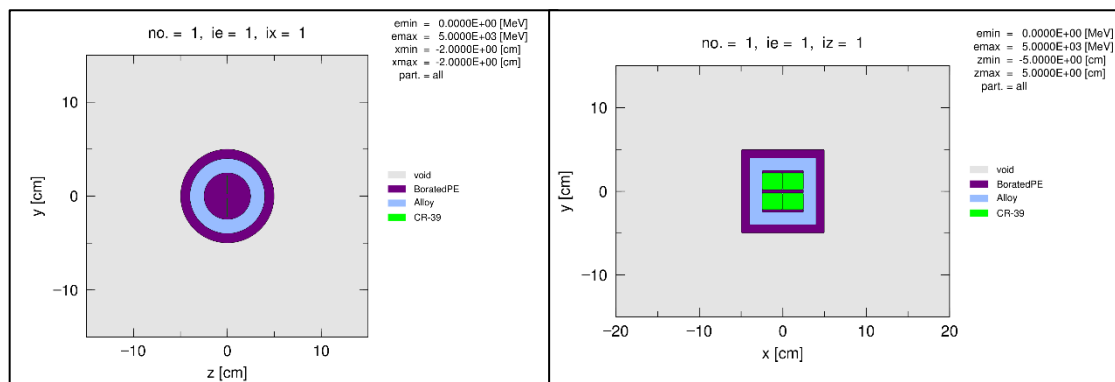


Figure 5.4 The geometry of CUMOD in PHITS

To get the parallel neutron sources, as the same condition where the fluence-to- $H^*(10)$ conversion coefficient simulated, the neutron line source were selected and located 10 cm away from the surface of CUMOD. The example of the PHITS simulation is shown in Figure 5.5.

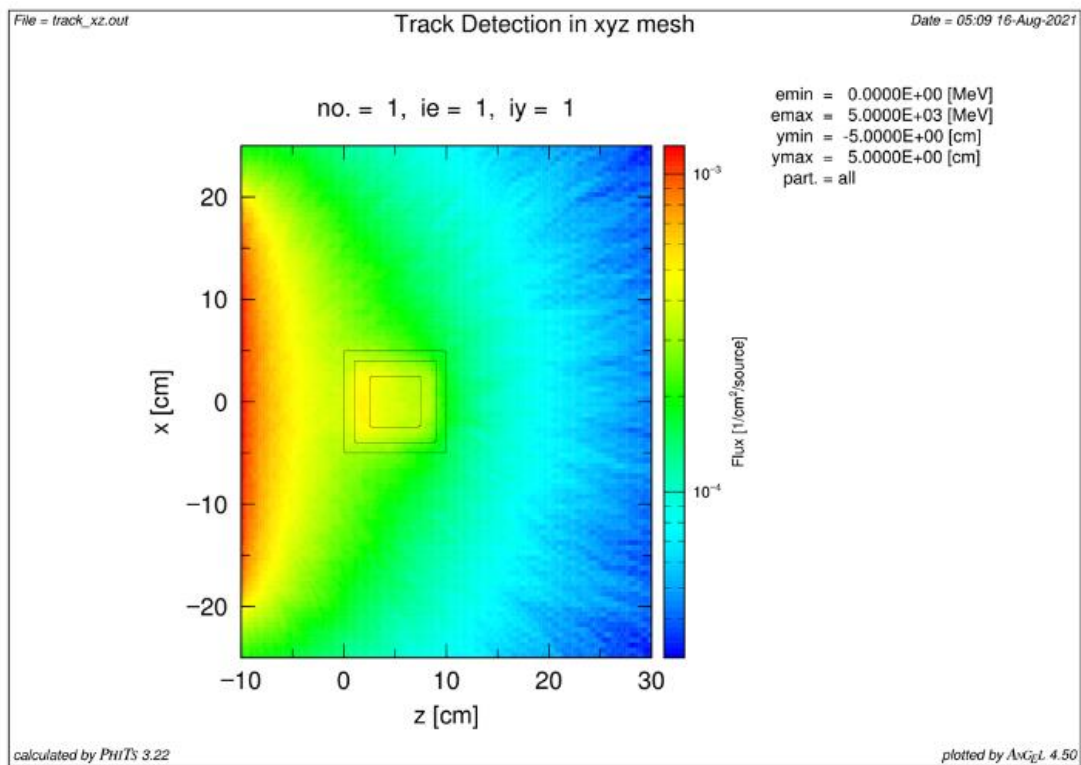


Figure 5.5 The example picture of the neutron source and CUMOD in PHITS

Table 5.2 The raw data for CUMOD response function

neutron energy (MeV)	Energy deposit [MeV/cm ³ /source]			No. of neutron
	Average	Standard deviation	Relative error	
1.00E-09	8.76E-06	2.83E-07	0.020	3.30E+08
1.00E-08	1.77E-05	2.51E-07	0.021	6.00E+08
2.00E-08	3.92E-05	1.05E-06	0.019	4.70E+08
3.00E-08	6.18E-05	1.74E-06	0.017	4.50E+08
4.00E-08	8.38E-05	1.54E-06	0.014	6.00E+08
5.00E-08	1.04E-04	1.93E-06	0.012	6.00E+08
7.50E-08	1.49E-04	1.74E-06	0.010	6.00E+08
1.00E-07	1.86E-04	2.22E-06	0.010	5.00E+08
1.00E-06	4.09E-04	3.45E-06	0.010	3.30E+08
1.00E-05	1.57E-04	2.26E-06	0.012	3.50E+08
1.00E-04	2.73E-04	3.98E-06	0.010	4.50E+08
1.00E-03	1.03E-04	1.07E-06	0.011	6.00E+08
1.00E-02	9.97E-05	9.67E-07	0.010	2.80E+08
1.00E-01	4.69E-04	2.13E-06	0.008	3.50E+07
2.00E-01	7.91E-04	7.69E-06	0.009	2.20E+07
3.00E-01	1.04E-03	9.92E-06	0.009	2.20E+07
4.00E-01	1.30E-03	2.03E-05	0.009	2.30E+07
5.00E-01	1.46E-03	2.41E-05	0.009	2.00E+07
7.50E-01	1.83E-03	1.53E-05	0.009	2.00E+07
1.00E+00	2.32E-03	3.97E-06	0.008	2.20E+07
2.00E+00	2.97E-03	9.37E-06	0.008	2.00E+07
3.00E+00	3.57E-03	2.17E-05	0.008	1.80E+07
4.00E+00	4.51E-03	4.40E-05	0.009	1.50E+07
5.00E+00	4.43E-03	3.98E-05	0.009	1.50E+07
7.50E+00	5.46E-03	1.67E-05	0.008	1.50E+07
1.00E+01	6.37E-03	4.99E-05	0.010	1.00E+07
1.40E+01	8.36E-03	7.18E-05	0.010	1.00E+07
2.00E+01	1.29E-02	1.28E-04	0.009	1.00E+07
3.00E+01	3.57E-03	2.17E-05	0.008	1.80E+07
4.00E+01	4.51E-03	3.93E-05	0.008	1.80E+07
5.00E+01	4.42E-03	2.47E-05	0.008	1.80E+07
7.50E+01	5.47E-03	5.32E-06	0.009	1.30E+07
1.00E+02	1.70E-02	2.49E-04	0.015	6.00E+08
2.00E+02	2.37E-02	5.51E-04	0.019	6.00E+08
2.50E+02	2.61E-02	5.13E-04	0.017	3.12E+08
5.00E+02	4.20E-02	4.57E-04	0.014	2.82E+08
1.00E+03	6.74E-02	1.18E-03	0.016	1.27E+08

With the value from Table 5.2, the average energy deposited from the 4 CR-39 was considered as the response of CUMOD to each neutron energy. The relative response function of CUMOD to 4.5 MeV neutron, as average energy of $^{241}\text{AmBe}$, is illustrated in Figure 5.6.

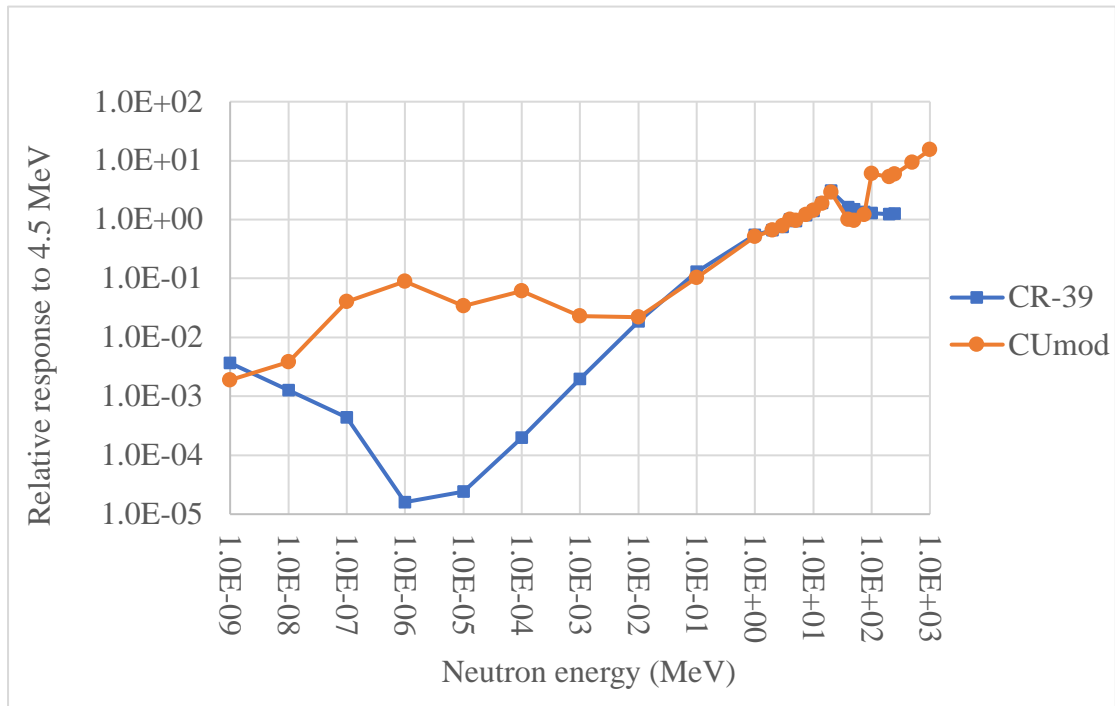


Figure 5.6 The response function of CUMOD and CR-39 from PHITS

The same simulation method was applied to bared CR-39 to see the response function also. According to the specification of CR-39, the response energy range of 200 keV to 14 MeV were increased up to the required neutron energy range of this study.

5.4 Validation of CUMOD response function

The validation of CUMOD response function results based on the known neutron spectrum starts from the classification of the neutron fluence into each equal neutron energy bin. The number of neutrons were normalized so that the integral is equal 1. The response function was then convolved to the neutron fluence.

For the neutron energy range of 10 eV to 15 MeV, the reported neutron spectrum with percent different of CUMOD response function has illustrated in Figure 5.7. There are 3 neutron energy intervals of 0.001, 0.1 and 1 MeV with the different percentage of -75.1%, -64.1% and -19.4%, respectively. With the weighting of neutron fluence of 0.3, 0.6 and 0.1 for the corresponding neutron energy. The total approximation of difference percentage could be about 60%.

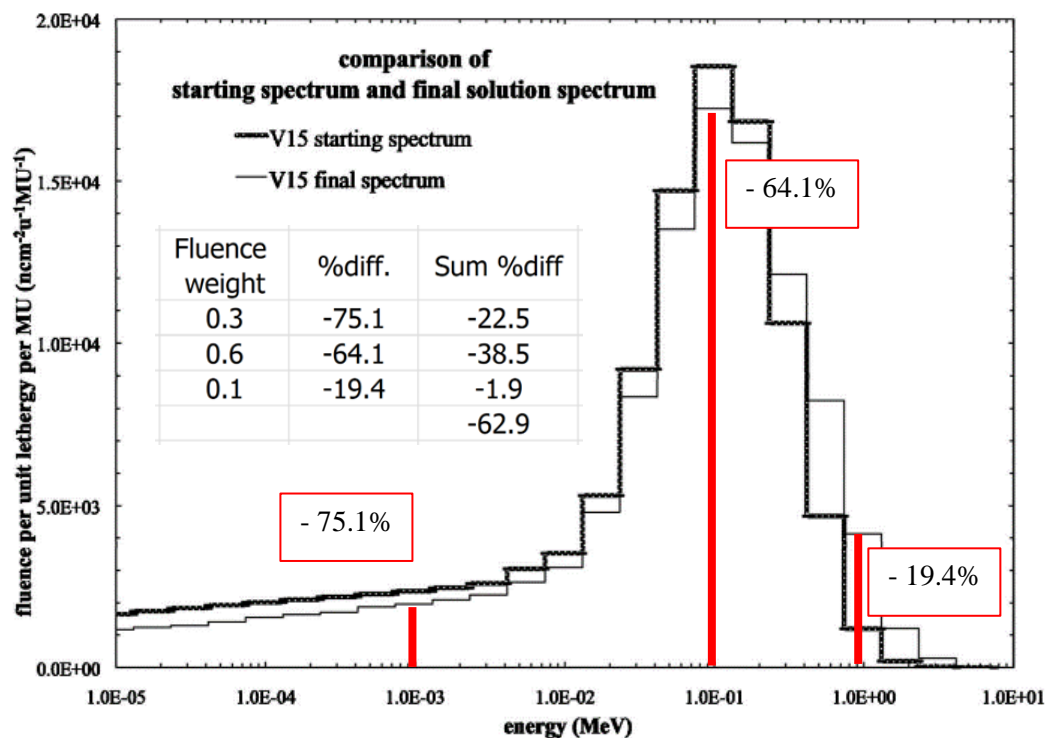


Figure 5.7 The reported neutron spectrum up to 15 MeV with percent different of CUMOD response function, the inlay picture shows the approximation of different percentage

The result of $H^*(10)$ per monitor unit (MU) from CUMOD was $0.7 \mu\text{Sv}/\text{MU}$ which was about 40% lower than $1.1 \mu\text{Sv}/\text{MU}$ from Howell et al. study, as shown in

Figure 5.8. When compared to the approximation difference percentage, the $H^*(10)$ result from CUMOD was overestimated about 20% for the neutron energy range of 10 eV to 15 MeV.

Plan	reference	Irradiation	ref.(μSv)	CUMOD $H^*(10)$			% difference
				Average	SD	$H^*(10)/\text{MU}$	
15MV 1.1 $\mu\text{Sv}/1\text{MU}$	Howell, 2009	2000 MU	2200	1312.9	786.7	0.7	-40.3

Figure 5.8 The CUMOD $H^*(10)$ result from 15 MeV linaca

For the high energy neutron, up to 140 MeV, the reported neutron spectrum with percent different of CUMOD response function has illustrated in Figure 5.9. There are 5 neutron energy intervals of 10^{-8} , 0.1, 1, 20 and 50 MeV with the different percentage of -92.2%, -64.1%, -19.4%, 30.5% and -43%, respectively. With the weighting of neutron fluence of 0.1, 0.1, 0.3, 0.2 and 0.3 for the corresponding neutron energy, the total approximation of difference percentage could be 28.3%.

The result of $H^*(10)/\text{proton Gy}$ from CUMOD was 3.1 $\mu\text{Sv}/\text{Gy}$ which was comparable to 3.2 $\mu\text{Sv}/\text{Gy}$ from Trinkl et. al. study, as shown in Figure 5.10. When compared to the approximation difference percentage, the $H^*(10)$ result from CUMOD was overestimated about 25% for the neutron energy range up to 140 MeV.

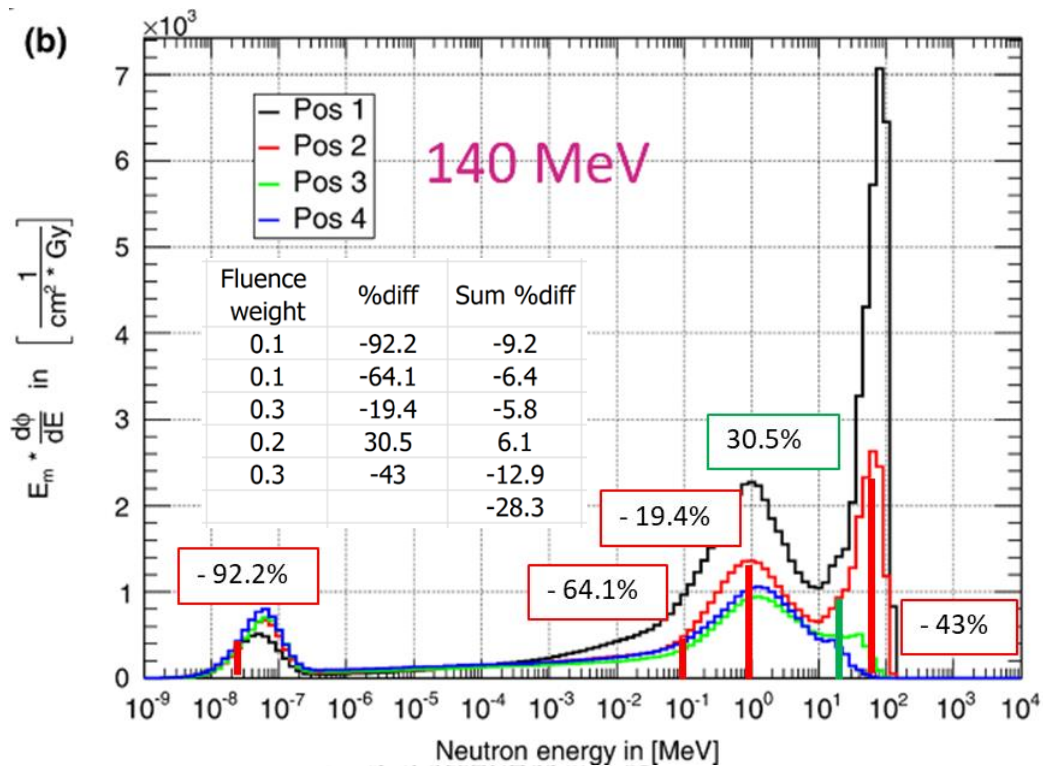


Figure 5.9 The reported neutron spectrum up to 140 MeV with percent different of CUMOD response function, the inlay picture shows the approximation of different percentage

Plan	reference	Irradiation	ref.(μ Sv)	CUMOD $H^*(10)$			% difference
				Average	SD	$H^*(10)/\text{Gy}$	
140 MeV 3.2 μ Sv/Gy	Trinkl, 2017	80 Gy	256	246.3	88.2	3.1	-3.8

Figure 5.10 The CUMOD $H^*(10)$ result from irradiated with 140 MeV proton beam for the field size of $11 * 11 \text{ cm}^2$

For the high energy neutron, up to 200 MeV, the reported neutron spectrum with percent different of CUMOD response function has illustrated in Figure 43. There are 6 neutron energy intervals of 10^{-8} , 0.1, 1, 20, 50 and 140 MeV with the different percentage of -92.2%, -64.1%, -19.4%, 30.5%, -43% and 46.9%, respectively. With the weighting of neutron fluence of 0.1, 0.1, 0.3, 0.15, 0.25 and 0.1 for the corresponding neutron energy. The total approximation of difference percentage could be 22.9%.

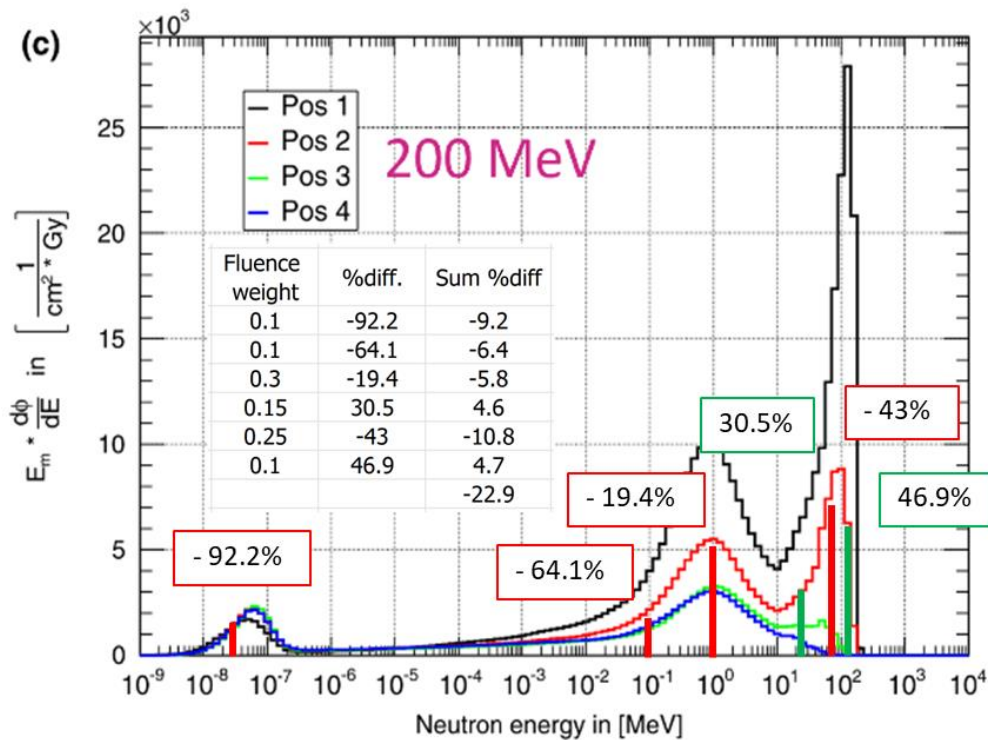


Figure 5.11 The reported neutron spectrum up to 200 MeV with percent different of CUMOD response function, the inlay picture shows the approximation of different percentage

The result of $H^*(10)$ /proton Gy from CUMOD was 13.7 $\mu\text{Sv}/\text{Gy}$ which was higher than 11 $\mu\text{Sv}/\text{Gy}$ from Trinkl et. al. study about 25%, as shown in Figure 5.12. When compared to the approximation difference percentage, the $H^*(10)$ result from CUMOD was overestimated about 50% for the neutron energy range up to 200 MeV.

Plan	reference	Irradiation	ref.(μSv)	CUMOD $H^*(10)$			% difference
				Average	SD	$H^*(10)/\text{Gy}$	
200 MeV 11 $\mu\text{Sv}/\text{Gy}$	Trinkl, 2017	30 Gy	330	411.6	290.2	13.7	24.7

Figure 5.12 The CUMOD $H^*(10)$ result from irradiated with 200 MeV proton beam for the field size of $11 \times 11 \text{ cm}^2$ (30 Gy)

5.5 Ambient dose equivalent measurements

The results from WENDI-II and CUMOD for single energy dose plane and multiple energy volume when irradiated with the proton dose 5 Gray-Equivalent (GyE) are illustrated in Table 5.3. For single energy plan dose, The $H^*(10)$ from WENDI-II was 37, 176 and 381 μSv for the depth of 10, 20 and 30 cm, respectively. While the $H^*(10)$ from CUMOD was 109 and 222 μSv for the depth of 20 and 30 cm, respectively. For the depth of 10 cm, the $H^*(10)$ value does not meet the minimum detectability of CR-39 that is the reason of N/A for CUMOD.

Table 5.3 The ambient dose equivalent from WENDI-II and CUMOD for single energy dose plane and multiple energy volume.

Plan type	Depth (cm)	WENDI-II	CUMOD		% Difference
		$H^*(10)$ (μSv)	$H^*(10)$ (μSv)	SD	
Plane	10	37	N/A	N/A	N/A
	20	176	109	104	38
	30	381	222	105	42
Volume	10	139	91	87	35
	20	337	239	159	29
	30	758	526	421	31

For, The $H^*(10)$ from WENDI-II was 139, 337 and 758 μSv for the depth of 10, 20 and 30 cm, respectively. While the $H^*(10)$ from CUMOD was 91, 159 and 421 μSv for the depth of 10, 20 and 30 cm, respectively. The Figure 5.13 presents the track characteristic of single energy dose plane multiple energy volume plan at 30 cm depth with the proton dose of 5GyE. The increasing of the number of tracks was observed for the volume plan.

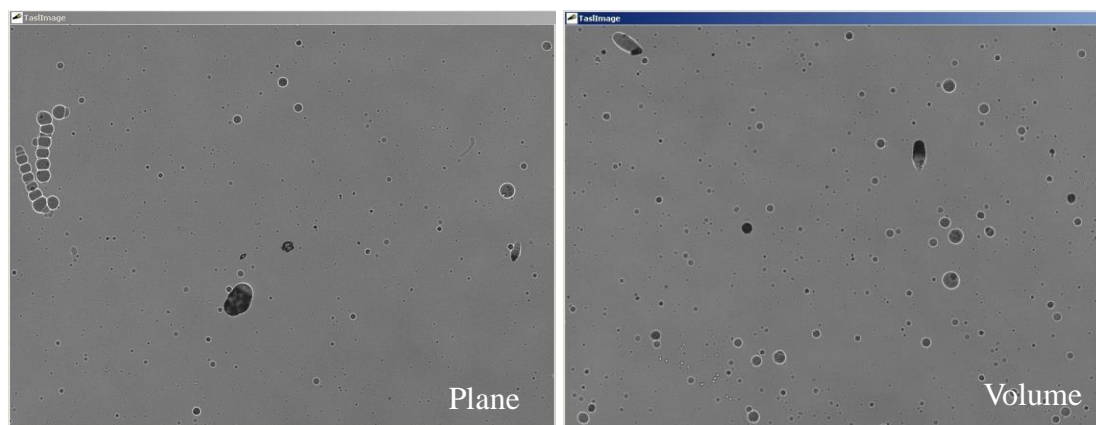


Figure 5.13 The characteristic of the particle tracks from different plan types

The additional test was the variation of the proton dose for single energy plan. The single energy plan for 30 cm depth was selected and irradiated with the proton dose of 2, 5 and 10 GyE. The result was shown in Table 8. The $H^*(10)$ from WENDI-II was 149, 381 and 770 μSv for the proton dose of 2, 5 and 10 GyE, respectively. While the $H^*(10)$ from CUMOD was 113, 222 and 467 μSv for the proton dose of 2, 5 and 10 GyE, respectively.

Table 5.4 The ambient dose equivalent from WENDI-II and CUMOD for single energy dose plane with variation on the proton dose

Plan type	Depth (cm)	Proton dose (GyE)	WENDI-II	CUMOD		% Difference
			$H^*(10)$ (μSv)	$H^*(10)$ (μSv)	SD	
Plane	30	2	149	113	74	24
		5	381	222	105	42
		10	770	467	140	39

CHAPTER 6 DISCUSSION

The maximum difference of $H^*(10)$ between the WENDI-II and CUMOD, according to Table 7 and 8 was about 40%. The reason might be explained with the energy response function. For the accomplished measurement of neutron ambient dose equivalent, it is necessary to understand the neutron energy spectrum at the measurement location. Along the neutron spectrum, Trinkl et. al.⁽¹⁷⁾ showed that there are a few neutron peaks observed around medium target, the evaporation peak (0.1 – 19.6 MeV) and the high energy peak (>19.6 – 250 MeV). The difference between the WENDI-II and CUMOD response function over these energy ranges was considered, as presented in Figure 6.1. The two under-estimate ranges of CUMOD were observed in this study.

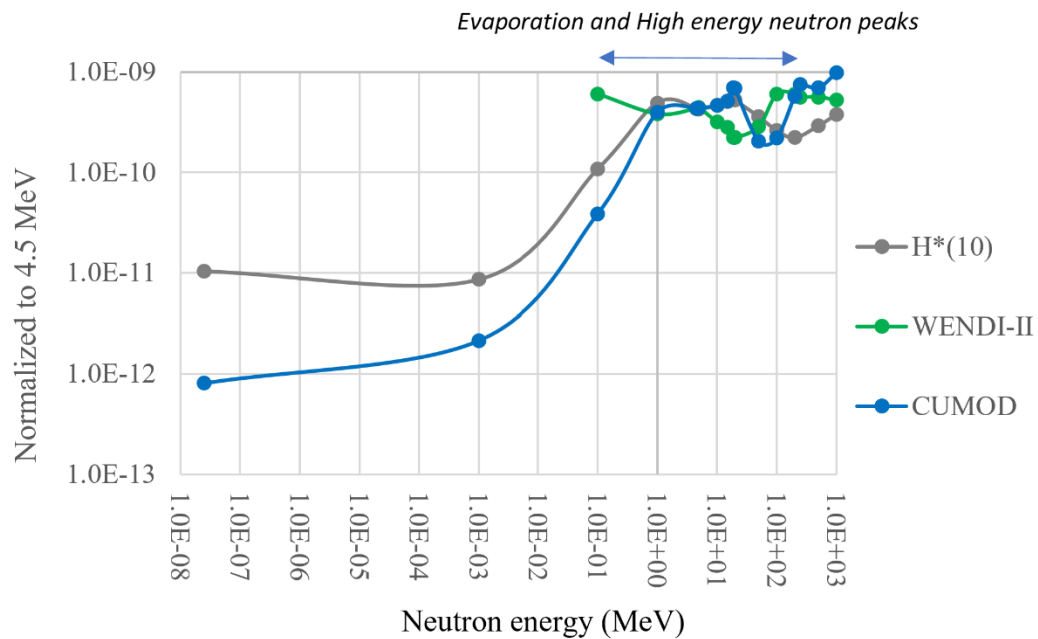


Figure 6.1 The response function of CUMOD (circle), $H^*(10)$ conversion coefficient (diamond) and WENDI-II (cross).

The relatively high standard deviation was observed similarly to the report of Infantino et al.⁽²⁴⁾ study. It might be the summing up of the nature of CR-39 detector and un-intended design of the automatic reader system for the moderator as CUMOD. However, the plotted of the $H^*(10)$ from WENDI-II and CUMOD was revealed the linear relationship between these two detectors, as demonstrated in Figure 6.2. We might estimate the $H^*(10)$ as WENDI-II measured from what obtained from CUMOD using the factor of 0.6437.

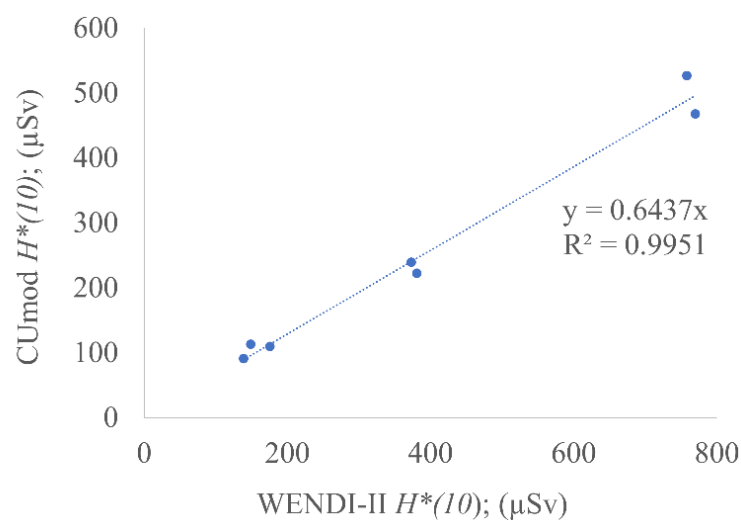


Figure 6.2 The linear relationship $H^*(10)$ between WENDI-II and CUMOD

From the validation of CUMOD neutron response function, both CUMOD and WENDI-II were used to measure the $H^*(10)$ at the same location, as Howell et. al. and Trinkl et. al. studies. The results are shown in Figure 6.3. The $H^*(10)/\text{MU}$ for 15 MeV linac beam and $H^*(10)/\text{Gy}$ from CUMOD and WENDI-II were in the same range with these two studies. The CUMOD response function overestimated the $H^*(10)$ up to about 50% for the neutron energy range of 10 eV to 200 MeV.

Plan	reference	Irradiation	ref. (μSv)	CUMOD H*(10)			WENDI-II H*(10)				
				Average	SD	$\mu\text{Sv/Gy}/(\text{MU})$	% diff	neutron	8% sensitivity (after 2 years)	$\mu\text{Sv/Gy}/(\text{MU})$	% diff
15MV 1.1 $\mu\text{Sv}/\text{MU}$	Howell et. Al.	2000 MU	2200	1312.9	786.7	0.66	-40.3	1560.0	1684.8	0.84	-23.4
140 MeV 3.2 $\mu\text{Sv}/\text{Gy}$	Trinkl et. Al. at 45°, 2m FS 11 x 11 cm ²	80 Gy	256	246.3	88.2	3.1	-3.8	428.0	462.2	5.8	80.6
200 MeV 11 $\mu\text{Sv}/\text{Gy}$	Phantom 30x30x30 cm ³	30 Gy	330	411.6	290.2	13.7	24.7	463.5	500.6	16.7	51.7

Figure 6.3 The validation results of CUMOD neutron response function

The ambient dose equivalent per therapeutic dose, $\frac{H^*(10)}{D}$ (mSv/Gy) was also presented in Table 6.1 with the purpose of comparing to other studies. This value depends on many factors such as the design of the nozzle, volume of irradiation, medium, measured distance and surrounded environment. The $\frac{H^*(10)}{D}$ of WENDI-II was in the range of 0.007 to 0.152 mSv/Gy. For the $\frac{H^*(10)}{D}$ of CUMOD, the value was varied from 0.018 to 0.105 mSv/Gy. When considering the result of proton dose variation, the observation of $\frac{H^*(10)}{D}$ of both WENDI-II and CUMOD was almost constant.

Table 6.1 The comparison of the ambient dose equivalent per therapeutic dose from WENDI-II and CUMOD to Charyyev et al.

Plan type	Depth (cm)	Proton dose (GyE)	$H^*(10)/D$ (mSv/Gy)		
			WENDI-II	CUMOD	Charyyev et al.
Plane	10	5	0.007	N/A	0.001 to 0.242
	20	5	0.035	0.022	
	30	2	0.075	0.057	
		5	0.076	0.044	
		10	0.077	0.047	
Volume	10	5	0.028	0.018	
	20	5	0.067	0.048	
	30	5	0.152	0.105	

The comparison of $\frac{H^*(10)}{D}$ results were compared with Charyyev et al.⁽²⁵⁾, where the measurement was accomplished with the field size of 9 * 9 cm² and at the distance of 105 cm. The $\frac{H^*(10)}{D}$ was presented in the range of 0.001 to 0.242 mSv/Gy for various position. In our study, the measurement was performed with the field size of 10 * 10 cm² and at the distance of 100 cm. The $\frac{H^*(10)}{D}$ from both the plane and volume plan type were in the same range to Charyyev study. The effect of the different in the measurement conditions such as the field size, the measured distance and the position angle was included in this comparison.

CHAPTER 7

CONCLUSIONS

In this study, the objective is to create and validate the new moderated neutron detector for the determination of the accumulated ambient dose equivalent, $H^*(10)$, in the proton therapy.

The CUMOD calibration with $^{241}\text{AmBe}$ demonstrated the linear response, except for the high $H^*(10)$ of 1000 μSv . The $^{241}\text{AmBe}$ dose calibrator was in the same laboratory that provided the service of detector calibration. The unoccupied of the room is quite rare.

The validation of CUMOD response function using 15 MeV photon beam from Linac and 140 MeV and 200 MeV beam from proton therapy shown the overestimation of $H^*(10)$ about 50%. The using of mono-energetic neutron beam, which is the ideal for response function validation, is the limitation in this study.

The measured $H^*(10)$ from CUMOD, even with the maximum different of 40%, could be calculated to substitute with the value from the broad recognized neutron detector (WENDI-II). The validation of CUMOD against the WENDI-II confirm that the CUMOD, as the passive detector, could be used well for $H^*(10)$ measurement in proton therapy.

The further study in various clinical conditions of $H^*(10)$ measurement will be more revealed the sustainability of using CUMOD in proton therapy center. The knowledge of neutron spectrum might be the superior choice for CUMOD validation. So, the simulation of neutron spectrum or the measurement using Bonner sphere detector system could be more accurate.

REFERENCES

1. Brenner, D. J. and Hall, E. J. Secondary neutrons in clinical proton radiotherapy: a charged issue. *Radiother Oncol.* **86**(2), 165-70 (2008).
2. Pelliccioni, M. Overview of Fluence-to-Effective Dose and Fluence-to-Ambient Dose Equivalent Conversion Coefficients for High Energy Radiation Calculated Using the FLUKA Code. *Radiation Protection Dosimetry.* **88**(4), 279-297 (2000).
3. Sokolov, A., Fehrenbacher, G. and Radon, T. Design DEVELOPMENT OF A PASSIVE NEUTRON DOSEMETER FOR THE USE AT HIGH-ENERGY ACCELERATORS. *Radiation Protection Dosimetry.* **170**(1-4), 195-198 (2016).
4. Fehrenbacher, G., Kozlova, E., Gutermuth, F., Radon, T., Schütz, R., Nolte, R. and Böttger, R. Measurement of the fluence response of the GSI neutron ball dosimeter in the energy range from thermal to 19 MeV. *Radiation Protection Dosimetry.* **126**(1-4), 546-548 (2007).
5. Fehrenbacher, G., Gutermuth, F., Kozlova, E., Radon, T., Aumann, T., Beceiro, S., Le Bleis, T., Boretzky, K., Emling, H., Johansson, H. et al. Measurement of the fluence response of the GSI neutron ball in high-energy neutron fields produced by 500 AMeV and 800 AMeV deuterons. *Radiation Protection Dosimetry.* **126**(1-4), 497-500 (2007).
6. Vanaudenhove, T., Dubus, A. and Pauly, N. Comparing Geant4 hadronic models for the WENDI-II rem meter response function. *Radiation Protection Dosimetry.* **154**(3), 340-345 (2012).
7. Olsher, R. H. and McLean, T. D. High-energy response of the PRESCILA and WENDI-II neutron rem meters. *Radiation Protection Dosimetry.* **130**(4), 510-513 (2008).
8. Paganetti, H. and Bortfeld, T. *Proton Therapy.* (Berlin, Heidelberg: Springer Berlin Heidelberg) (2006) ISBN 978-3-540-29999-8.
9. Niemierko, A. *Biological Optimization.* (Berlin, Heidelberg: Springer Berlin Heidelberg) (2006) ISBN 978-3-540-30356-5.
10. Delaney, C. P., Zutshi, M., Senagore, A. J., Remzi, F. H., Hammel, J. and Fazio, V. W. Prospective, randomized, controlled trial between a pathway of controlled rehabilitation with early ambulation and diet and traditional postoperative care after laparotomy and intestinal resection. *Dis Colon Rectum.* **46**(7), 851-9 (2003).
11. Newhauser, W. D. and Zhang, R. The physics of proton therapy. *Physics in Medicine and Biology.* **60**(8), R155-R209 (2015).
12. *Neutrons, Fission, and Criticality.* (2007).
13. Allisy, A., Jennings, W. A., Kellerer, A. M. and Müller, J. W. Part I Quantities and Units for Measurement and Calculation in Radiation Protection. *Reports of the International Commission on Radiation Units and Measurements.* **os-26**(2), 3-8 (1993).
14. ICRP Conversion Coefficients for use in Radiological Protection against External Radiation. ICRP Publication 74. *Ann. ICRP* **26** (3-4)(1996).
15. Fiechtner-Scharrer, A., Mayer, S., Boschung, M. and Whitelaw, A. Influence of variation of etching conditions on the sensitivity of PADC detectors with a new evaluation method. *Radiat Prot Dosimetry.* **144**(1-4), 150-4 (2011).
16. Satoh, D., Maeda, Y., Tameshige, Y., Nakashima, H., Shibata, T., Endo, A., Tsuda, S., Sasaki, M., Maekawa, M., Shimizu, Y. et al. Shielding study at the Fukui Prefectural Hospital Proton Therapy Center. *Journal of Nuclear Science and*

Technology. **49**(11), 1097-1109 (2012).

17. Trinkl, S., Mares, V., Englbrecht, F. S., Wilkens, J. J., Wielunski, M., Parodi, K., Rühm, W. and Hillbrand, M. Systematic out-of-field secondary neutron spectrometry and dosimetry in pencil beam scanning proton therapy. *Medical physics*. **44**(5), 1912-1920 (2017).

18. Shamsuzzaman, M., Rahman, M. and Siddiqua, T. Standardization of ^{241}Am -Be Neutron Radiation Field to Characterize the moderated (9") Neutron Detector. *International Journal of Current Research*. **11**, 5714-5720 (2019).

19. De Smet, V., Stichelbaut, F., Vanaudenhove, T., Mathot, G., De Lentdecker, G., Dubus, A., Pauly, N. and Gerardy, I. Neutron $\text{H}^*(10)$ inside a proton therapy facility: comparison between Monte Carlo simulations and WENDI-2 measurements. *Radiat Prot Dosimetry*. **161**(1-4), 417-21 (2014).

20. Lee, S., Lee, C., Shin, E. H., Cho, S., Kim, D. H., Han, Y., Choi, D. H., Ye, S. J. and Kim, J. S. Measurement of Neutron Ambient Dose Equivalent in Proton Radiotherapy with Line-Scanning and Wobbling Mode Treatment System. *Radiat Prot Dosimetry*. **177**(4), 382-388 (2017).

21. Matsumoto, S. and Yonai, S. EVALUATION OF NEUTRON AMBIENT DOSE EQUIVALENT IN INTENSITY-MODULATED COMPOSITE PARTICLE THERAPY. *Radiation Protection Dosimetry*. **193**(2), 90-95 (2021).

22. Jägerhofer, L., Tree, J., Forkel-Wirth, D., Theis, C., Vincke, H., Iwamoto, Y., Hagiwara, M., Satoh, D., Iwase, H., Yashima, H. et al. Characterization of the WENDI-II REM Counter for its Application at MedAustron. *Progress in Nuclear Science and Technology*. **2**(2011).

23. Howell, R. M., Kry, S. F., Burgett, E., Hertel, N. E. and Followill, D. S. Secondary neutron spectra from modern Varian, Siemens, and Elekta linacs with multileaf collimators. *Medical physics*. **36**(9), 4027-38 (2009).

24. Infantino, A., Cicoria, G., Lucconi, G., Pancaldi, D., Vichi, S., Zagni, F., Mostacci, D. and Marengo, M. Radiation Protection Studies for Medical Particle Accelerators using Fluka Monte Carlo Code. *Radiation Protection Dosimetry*. **173**(1-3), 185-191 (2016).

25. Charyyev, S. and Wang, C.-K. C. ASSESSMENT OF AMBIENT NEUTRON DOSE EQUIVALENT IN SPATIALLY FRACTIONATED RADIOTHERAPY WITH PROTONS USING PHYSICAL COLLIMATORS. *Radiation Protection Dosimetry*. **189**(2), 190-197 (2020).

26. Kessel, R., Kacker, R. N. and Sommer, K.-D. Uncertainty budgeting for range calibration. *Measurement*. **45**(6), 1661-1669 (2012).

27. Available at <http://www.conceptualphysicstoday.com/2015/02/americium-241beryllium-radioactive.html>.

APPENDIX I

Data of CUMOD for PHITS

Data for the of PHITS Monte Carlo simulation

```

1 [ T i t l e ]
2 CUMOD response function
3
4 [ P a r a m e t e r s ]
5  icntl   =           8      # (D=0) 3:ECH 5:NOR 6:SRC 7,8:GSH 11:DSH 12:DUMP
6  maxcas  =          10000   # (D=10) number of particles per one batch
7  maxbch  =           60000   # (D=10) number of batches
8  file(1) = c:/phits        # (D=c:/phits) PHITS install folder name
9  file(6) = phits.out       # (D=phits.out) general output file name
10 istdev  =             2
11
12 [ S o u r c e ]
13  s-type  = 1                # mono-energetic axial source
14  proj    = neutron         # kind of incident particle
15  dir     = all             # z-direction of beam [cosine]
16  r0      = 10.            # radius [cm]
17  z0      = -15.           # minimum position of z-axis [cm]
18  z1      = -15.           # maximum position of z-axis [cm]
19  e0      = 250            # energy of beam [MeV/u]
20
21 [ M a t e r i a l ]
22 mat[1]   H  1.36784d-1      $1.04 g/cm3  #5% borated polyethylene, B4C in (C2H4)n
23         B  4.8257d-2
24         C  8.14959d-1
25 MT1     poly.20t
26 mat[2]   Cd 1d-1           $9.38 g/cm3 #alloy,Cd-Sn-Pb-Bi
27         Sn 1.33d-1
28         Pb 2.67d-1
29         Bi 5d-1
30 MT2     poly.20t
31 mat[3]   H  3.24d-1        $1.3 g/cm3  #CR-39
32         C  4.97d-1
33         O  1.79d-1
34 MT3     poly.20t
35
36 [ M a t N a m e C o l o r ]
37   mat  name                color
38   1    BoratedPE          purple
39   2    Alloy              pastelblue
40   3    CR-39              green
41
42 [ S u r f a c e ]
43 10 so 100                  $ outer
44 11 RCC -5 0 0 10 0 0 5.0  $ outerBoratedPE
45 12 RCC -4 0 0 8 0 0 4.0   $ alloy layer
46 13 RCC -2.5 0 0 5 0 0 2.5 $ innerBoratedPE
47 14 BOX 0 -2.2 -0.05 2.5 0 0 0 2 0 0 0 0.1 $ cr39UR
48 15 BOX 0 0.2 -0.05 2.5 0 0 0 2 0 0 0 0.1 $ cr39UL
49 16 BOX -2.5 -2.2 -0.05 2.5 0 0 0 2 0 0 0 0.1 $ cr39LR
50 17 BOX -2.5 0.2 -0.05 2.5 0 0 0 2 0 0 0 0.1 $ cr39LL
51
52
53 [ C e l l ]
54 100 -1 10                  $ outer region
55 101 1 -1.04 -11 12 13 14 15 16 17 $ outer BoratedPE
56 102 2 -9.38 -12 13 14 15 16 17 $ alloy layer
57 103 1 -1.04 -13 14 15 16 17 $ inner BoratedPE
58 104 3 -1.3 -14            $ upper right
59 105 3 -1.3 -15            $ upper left
60 106 3 -1.3 -16            $ lower right
61 107 3 -1.3 -17            $ lower left
62 110 0 -10 11 12 13 14 15 16 17 $ void
63

```

```

64 [ T - Deposit ]
65     title = Energy deposition in reg mesh
66     mesh = reg # mesh type is region-wise
67     reg = 104 105 106 107
68     volume # combined, lattice or level structure
69     non     reg     vol # reg definition
70     1      104    0.2*0.25*0.1
71     2      105    0.2*0.25*0.1
72     3      106    0.2*0.25*0.1
73     4      107    0.2*0.25*0.1
74
75     unit = 1 # unit is [MeV/cm^3/source]
76     material = all # (D=all) number of specific material
77     output = dose # total deposit energy
78     axis = reg # axis of output
79     file = deposit_reg.out # file name of output for the above axis
80     part = all
81     gshow = 1 # 0: no 1:bnd, 2:bnd+mat, 3:bnd+reg 4:bnd+lat
82     epsout = 1 # (D=0) generate eps file by ANGEL
83
84 [ E n d ]

```



APPENDIX II

Uncertainty of CUMOD in $H^*(10)$ measurement

With 2 types of uncertainty⁽²⁶⁾, type A uncertainty is an “evaluation of a component of measurement uncertainty determined by a statistical analysis of measured quantity values obtained under defined measurement conditions.” And type B uncertainty is an “evaluation of a component of measurement uncertainty determined by means other than a type A evaluation of measurement uncertainty.”

For type A uncertainty, the repeatability and reproducibility from CUMOD measured 3 times with $^{241}\text{AmBe}$ source calibrator. From the total of 12 CR-39 plates, 3 plates were excluded due to poor reading status. The average number of tracks and percent standard deviation of 9 CR-39 plates were calculated. The uncertainty was calculated as $\frac{\%SD}{\sqrt{n}}$. For type B uncertainty, the calibration uncertainty from the calibration report was 20% with $k = 2$. The combination of type A and type B uncertainty and the expanded with $k = 2$ at 95% confidence are shown in Figure II.1.

Source of uncertainty	Standard uncertainty (1 SD)
Type A uncertainty	18.88
Type B uncertainty	
Calibration process	20% (k=2)
Combined standard uncertainty	21.36%
Expanded uncertainty (k=2, 95% confidence)	42.72%

Figure II.1 The uncertainty calculation of CUMOD

APPENDIX III

Characteristics of WENDI-II

For the initial use of WENDI-II detector, it is necessary to study the characteristics of this detector. The studies of linearity, dose rate dependence, angular dependence, and long-term stability were examined. The $^{241}\text{AmBe}$ source with the source strength of 30 mCi, approximate $H^*(10)$ rate of $0.66 \mu\text{Sv/hr}$ at 1 m (from $22 \mu\text{Sv/hr @ 1 m per 1 Ci}^{(27)}$), was used in all studies.

Linearity

WENDI-II was placed 0.3 m away from the source. The measurement duration of 5, 10, 15 minutes was observed 5 times. The setup and the result were shown in Figure III.1. The approximate $H^*(10)$ rate at 30 cm was $7.33 \mu\text{Sv/hr}$ which equal to $0.61 \mu\text{Sv/5 minutes}$. The linearity response was observed with $R^2 = 0.9999$.

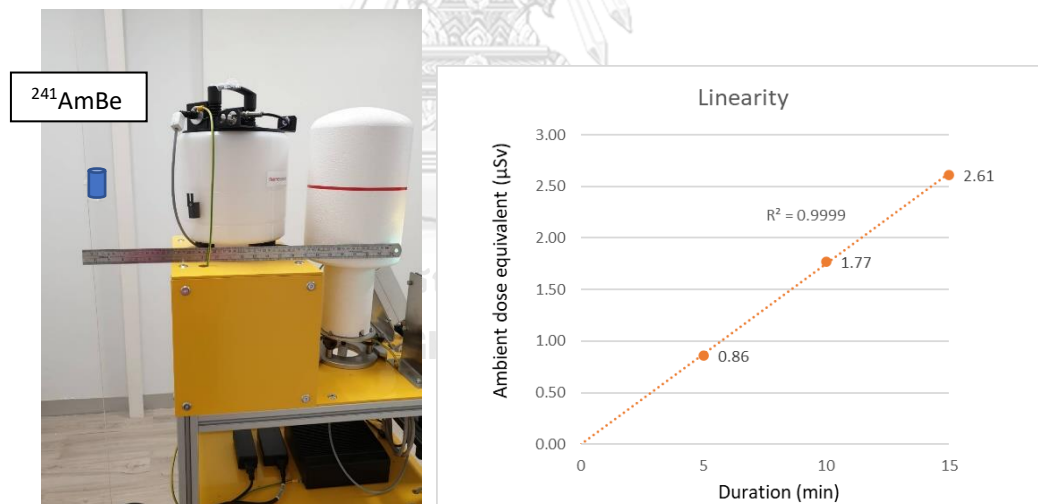


Figure III.1 The setup of WENDI-II and $^{241}\text{AmBe}$ (Right) and the linearity results (Left)

Dose rate dependence

For dose rate dependence study, WENDI-II measured the $H^*(10)$ for 5 minutes. By vary the distance of 0.3, 0.5, 1, 1.5 and 2 m, The measurement was repeated for 5 times. The result was shown in Figure III.2. The difference in the range of 20 to 50

percent was observed. With the larger $H^*(10)$, the percent difference for dose rate dependence decreased.

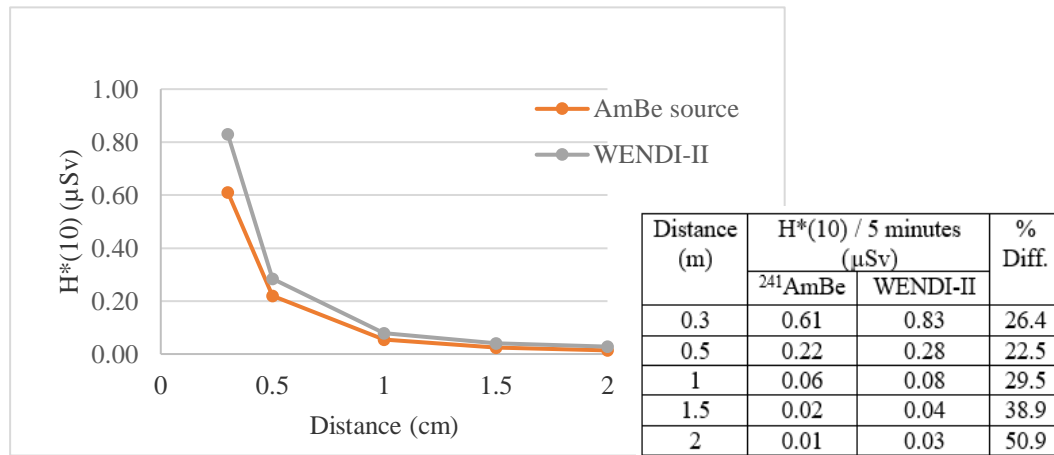


Figure III.2 The results of dose rate dependence. The inlay table presents the difference percentage.

Angular dependence

At the distance of 50 cm, the WENDI-II was rotated with the angle of -120 to 120 degree with 30-degree equi-angle. The measurement with duration of 5 minutes was repeated 3 times per study angle. The setup of WENDI-II and ²⁴¹AmBe was illustrated in Figure III.3.



Figure III.3 The setup for angular dependence study

The result of angular dependence was within 10%. The maximum angular dependence was found at the angle of 90-120 degree. The polar chart was demonstrated in Figure III.4.

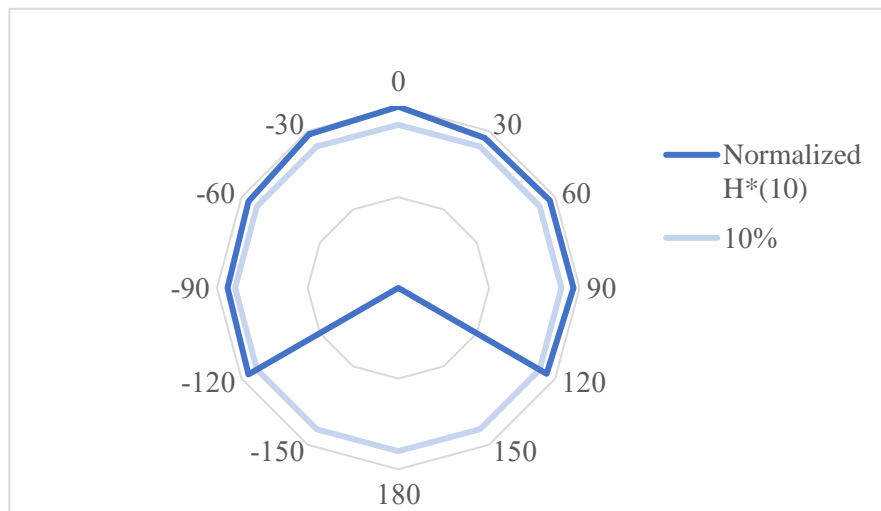


Figure III.4 The polar chart represents the angular dependence

Long-term stability

Over the study period of 6 months, the measurement of $H^*(10)$ at the distance of 30 cm, The Long-term stability was about 5% difference, as shown in Table III.1.

Table III.1 The Long-term stability of WENDI-II over 9 months

Elapsed months	Ambient dose equivalent (μSv)	
	Avg	% Diff.
0	0.86	0.00
6	0.83	-3.49
9	0.90	5.04

The higher reading at the 9th months might occurred due to the collection condition of the WENDI-II.

After studied the characteristic of WENDI-II, we found that WENDI-II is in good condition with the performance of the specification.

The sensitivity reduction

After 2 years of using WENDI-II for $H^*(10)$ measurements, the same $^{241}\text{AmBe}$ source was measured at the same 30 cm distance. The neutron $H^*(10)$ was 0.77 ± 0.02 μSv . The decay factor for 2 years is 0.9963. In overall, the sensitivity of WENDI-II was reduced about 8% which already included in 20% uncertainty. However, the recalibration of WENDI-II might be more suitable for the adjustment of the sensitivity.

In addition, to see the effect of inverse square law inside the proton treatment room, the measurement of $H^*(10)$ was accomplished at the position of 1, 3 and 5 m away from isocenter. The gantry was rotated at the 0 degree. The $30 * 30 * 35 \text{ cm}^3$ solid water phantom was laid up on the treatment couch and the surface was placed at the isocenter. The volume proton plan, $10 * 10 * 10 \text{ cm}^3$, the bottom depth of 30 cm, with the dose of 5 Gy was used in these experiments. The setup is shown in Figure III.5.

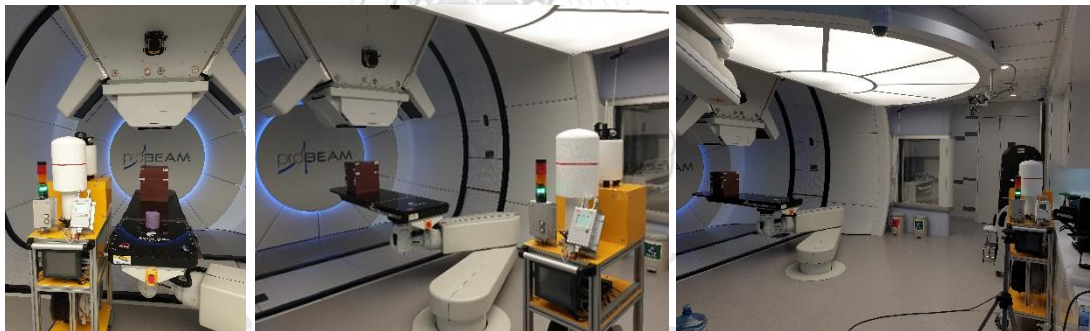


Figure III.5 The setup of WENDI-II at 100, 300 and 500 cm from isocenter

The results are shown in Table III.2. The parameters of the scatter from the environment contributed to the $H^*(10)$ results. The solid water phantom was not the only one secondary radiation source. It is the confirmation that inverse square law alone quite not suitable for $H^*(10)$ estimation.

Table III.2 The WENDI-II $H^*(10)$ results for inverse square law testing

distance (m)	Inverse square law factor	WENDI-II (μSv)	
		neutron	gamma
1	1	92	8.5
3	0.11	31	2.9
5	0.04	18	0.01

APPENDIX IV

Abstract for JSRT, 2018

The calculation of dose equivalent rate outside shielding in compact proton therapy facility

Introduction: The proton therapy project in King Chulalongkorn memorial hospital is a compact system with the capability of Intensity modulated proton therapy (IMPT) delivery. The shielding consideration is different from the old delivery technique in the terms of the neutron sources and facility size. To utilize the National council on radiation protection and measurement (NCRP) report no. 144 for shielding calculation of this facility, the radiation safety goal for surrounding occupational and public area should be achieved.

Methods: The calculation of dose equivalent outside shielding followed the suggestion in the publication was performed for this study purpose. The safety of the shielding was approved by expert before construction. The considered factors were the assumptions of the type of the tumor treating, number of patients, the workload, the beam direction, the occupancy factors and the composition of the shielding materials. The Moyer model was recommended in the guideline. The yield of neutrons and then the source strength was derived from the number of proton losses according to our statement which provided by vendor. The dose equivalent outside shielding at the console area was determined as the first interesting point.

Results: The maximum dose equivalent rate of 0.57 micro-Sievert per hour at the console area was observed for pelvic treatment. The highest tumor volume and energy used in the assumptions are the major causes. The summation of dose equivalent rate of all sites from this study and the value from vendor were 1.66 and 2.11 micro-Sievert per hour, respectively. The difference may attribute from the dissimilarity in the parameters and equations used. The full calculation and/or the Monte Carlo simulation on the other part of the shielding must be accomplished.

Keywords: IMPT shielding, compact proton, radiation protection

APPENDIX V

Abstract for AOCMP, 2020

The preliminary survey report of the compact proton therapy unit

Introduction: The number of compact proton therapy center is rapidly increasing. Her Royal Highness Princess Chakri Sirindhorn Proton Therapy center located at King Chulalongkorn Memorial hospital is the one which will be operating by early 2021. The radiation safety of shielding and operation must be considered.

Purpose: To verify the efficiency of the shielding and create the guideline for the treatment room entering after beam off at Her Royal Highness Princess Chakri Sirindhorn Proton Therapy center by measuring the ambient dose equivalent.

Methods: The proton beam energy of 230 MeV was delivered to the water phantom at the isocenter with the current about 2 nA. The Wendi II was used to measure the ambient dose equivalent both outside and inside the treatment room. Outside the treatment room, the measurements were performed in front of the shielding door, the control room, and the service engineer room. Inside the treatment room, the ambient dose equivalent was measured beside the treatment couch, 140 cm away from the isocentre. The measurement was prolonged for 6 minutes to observe the possible value.

Results: The ambient dose equivalent outside the treatment room was about the background, 0.5 $\mu\text{Sv/hr}$, for all measurement points. For the treatment room, the ambient dose equivalent after the beam off 1, 2, 3, 4, 5 and 6 minutes were 40.86, 1.17, 0.93, 0.78, 0.66, and 0.58 $\mu\text{Sv/hr}$, respectively.

Conclusion: For outside the treatment room, the shielding efficiency was under the shielding constrain of 1 mSv/year at the measured condition. The recommendation of the guideline for room entering after beam off was at least 2 minutes where the ambient dose equivalent was lower than 1.17 $\mu\text{Sv/hr}$ to achieve the personal dose limit lower than 5 mSv/year.

Keywords: Compact proton therapy, Ambient dose equivalent, the personal dose limit

VITA

NAME Tanawat Tawonwong

DATE OF BIRTH 11 August 1981

PLACE OF BIRTH Trat

INSTITUTIONS ATTENDED Mahidol University, 2003
Bachelor of Sciences
(Radiological Technology)

Mahidol University, 2011
Master of Sciences
(Medical Physics)

Chulalongkorn University, 2022
Doctor of Philosophy
(Medical Physics)

HOME ADDRESS 41 Nawamin14 Yak23, Bangkapi Bangkok
10240, Thailand

PUBLICATION The calculation of dose equivalent rate
outside shielding in compact proton therapy
facility (Oral presentation), The 74th
Annual Meeting of Japanese Society of
Radiological Technology (JSRT), 2018,
Japan

The preliminary survey report of the
compact proton therapy unit (Oral
presentation), The 20th Asia-Oceania
Congress on Medical Physics (AOCMP),
2020, Thailand